Calcium-dependent neuroepithelial contractions expel damaged cells from the developing brain

Leah Herrgen, Oliver P. Voss and Colin J. Akerman*

Department of Pharmacology, University of Oxford, Mansfield Road, Oxford OX1 3QT, UK

*Correspondence: colin.akerman@pharm.ox.ac.uk

SUMMARY

Both developing and adult organisms need efficient strategies for wound repair. In adult mammals, wounding triggers an inflammatory response that can exacerbate tissue injury and lead to scarring. In contrast, embryonic wounds heal quickly and with minimal inflammation, but how this is achieved remains incompletely understood. Using *in vivo* imaging in the developing brain of *Xenopus laevis*, we show that ATP release from damaged cells and subsequent activation of purinergic receptors induce long-range calcium waves in neural progenitor cells. Cytoskeletal reorganization, and activation of the actomyosin contractile machinery in a Rho kinase-dependent manner, then lead to rapid and pronounced apical-basal contractions of the neuroepithelium. These contractions drive the expulsion of damaged cells into the brain ventricle within seconds. Successful cell expulsion prevents the death of nearby cells and an exacerbation of the injury. Cell expulsion through neuroepithelial contraction represents a mechanism for rapid wound healing in the developing brain.

SHORT TITLE

Neuroepithelial contractions expel damaged cells

INTRODUCTION

To ensure survival, living organisms need efficient mechanisms for containing and repairing tissue injury (Sonnemann and Bement, 2011). Wounds commonly result from mechanical trauma but can also develop from a variety of pathological conditions such as infection or toxin exposure (Crosby and Waters, 2010; Singer and Clark, 1999). One of the early steps in wound healing is the clearance of cellular debris and invading pathogens from the wound site. In adult mammals, this is accomplished by phagocytic cells that are recruited to the wound in the days and weeks following the injury. While important for fighting infection, the resultant inflammatory reaction can exacerbate the primary wound, slow the healing process, and increase the deposition of non-functional fibrotic tissue commonly known as a scar (Martin and Leibovich, 2005; Novo and Parola, 2008). In contrast, embryonic wounds can heal much more quickly (McCluskey and Martin, 1995; Whitby et al., 1991) and with absent or minimal inflammation and scarring (Larson et al., 2010; Naik-Mathuria et al., 2007). Calcium signaling has recently emerged as a central player in wound closure (Clark et al., 2009; Soto et al., 2013) and phagocyte recruitment (Razzell et al., 2013; Sieger et al., 2012) in embryonic tissues, but precisely how the efficiency of embryonic wound healing is achieved on a molecular and cellular level remains a tantalizing question which holds the potential to generate novel therapeutic approaches (Degen and Gourdie, 2012).

Not surprisingly, much research on wound healing in embryos has focused on the repair of skin wounds as the skin is the organ system most

directly exposed to the external environment (Bielefeld et al., 2013; Lo et al., 2012). However, internal organs are also affected by noxious stimuli, and imperfect wound healing in organs such as the heart or liver can have detrimental consequences for an organism's health and viability (Gurtner et al., 2008). In particular, traumatic brain injury during development can lead to a range of severe neurological disorders in later life if wound healing mechanisms are overwhelmed (Baethmann et al., 1996; Hayes et al., 2007; Leroy-Malherbe et al., 2006). In spite of this, very little is known about the mechanisms that contain and mend injury to the embryonic brain. Here we describe a mechanism that uses rapid neuroepithelial contractions to remove damaged cells from injured tissue and thereby protects the developing brain from an exacerbation of the primary injury after wounding.

RESULTS

Wounding induces calcium waves, tissue contractions and rapid expulsion of damaged cells from the developing brain

Given the role of calcium waves in mediating tissue responses to wounding (Clark et al., 2009; Razzell et al., 2013; Sieger et al., 2012; Soto et al., 2013), we established an *in vivo* experimental setup in which we could simultaneously image calcium activity and tissue dynamics following wounding in a neuroepithelium. In the developing brain of *Xenopus laevis*, the optic tectum is a major component of the midbrain (Figure 1A) and grows by addition of neurons from a posterior progenitor pool (Lázár, 1973; Straznicky and Gaze, 1972). As in other vertebrate systems such as the ventricular zone

of the cortex, tectal progenitor cells are organized in a neuroepithelium that lines the ventricle (Figure 1B). Neural progenitors are characterized by their radial morphology and processes that extend to both the pial and ventricular surfaces (Figure 1C). The nuclei of neighboring progenitor cells in different phases of their cell cycle are found at different apical-basal positions, giving the neuroepithelium a pseudostratified appearance (Sauer, 1935).

The optic tectum of stage 44-48 *Xenopus laevis* embryos was loaded with the calcium indicator Oregon Green BAPTA-1 (OGB-1) and animals were imaged using *in vivo* multiphoton microscopy (Figure 1D). A fine micropipette was used to deliver precise mechanical insults to the neuroepithelium and cells dying as a result of wounding were visualized by their uptake of the nucleic acid dye propidium iodide (PI), which is membrane impermeant and therefore excluded from live cells. The majority of mechanical insults (18/22) resulted in cell death events, where one or more cells died as a result of wounding (3.2 ± 0.4 PI^+ cells per insult). All mechanical insults that resulted in cell death events were associated with calcium waves (18/18), whereas stimuli that did not lead to cell death were not (4/4), indicating a strong correlation between these events ($p < 0.01$ in Fisher's exact test). Calcium waves were initiated immediately after wounding (Figures 1E-1J; Movie S1 available online), and imaging with high temporal resolution confirmed that they spread from the site of injury to neighboring progenitor cells (Figures S1A-S1N). They propagated at a speed of 9 ± 1 μm/s and covered a distance of 172 ± 16 μm, with 54 ± 4 cells participating in a calcium wave. Transients in individual cells reached their peak amplitude 10 ± 1 s after onset and lasted for 91 ± 11 s (n = 18 animals).

To our surprise, wound-induced calcium waves were consistently accompanied by rapid contractions along the apical-basal axis of the neuroepithelium (Figures 1E-1J; Movie S1). Tissue contractions started 23 ± 2 s after the insult, were largest 30 ± 2 s after starting, and lasted for 158 ± 6 s (n = 18 animals). They generated a 10 ± 1% reduction in epithelial thickness, which we define as contraction amplitude. Therefore, neuroepithelial contractions operate on a timescale of seconds, which is comparable to smooth muscle. Importantly, contractions in brain explants in which all surrounding tissue had been removed were indistinguishable from those in intact animals, generating the same contraction amplitude (84 ± 7% of contraction amplitude in control animals, n = 23 animals, p = 0.442 in Mann-Whitney U test). This confirmed that the contractions are a feature of the developing brain.

We were intrigued to find that following wounding, PI^+ dead cells were often expelled from the tissue into the ventricle simultaneously with a neuroepithelial contraction (Figures 1E-1J; Movie S1). Cell expulsions started 15 ± 2 s after the insult and the expelled area increased rapidly for 49 ± 8 s, after which it increased more slowly or stabilized (n = 18 animals). We observed two different types of cell expulsion, one where the entire cell body was removed from the tissue, and one where part of the cell body remained in the tissue (see below for details). The fact that live cells were not expelled but rather ‘snapped back’ into place after wounding indicated that expulsion was an active process acting selectively upon dead cells.

We then sought to define the developmental time window during which neuroepithelial contractions and cell expulsions operate in the developing

brain. We induced mechanical injury in the neuroepithelium of embryos between stages 44 and 50, corresponding to two weeks and four months of age (see Experimental Procedures for details), and found that neuroepithelial contractions (Figure S1O) and cell expulsions (Figure S1P) were present throughout the entire time period. This is consistent with previous findings that neural progenitors persist in the tectum until at least stage 54 of development (Straznicky and Gaze, 1972).

To further explore the idea that calcium waves and tissue contractions were induced by cells dying as a result of wounding, rather than by the mechanical insult itself, we sought to induce cell death by exposing the neuroepithelium to different noxious stimuli (Figure 1K).

First, in order to generate small wounds in a manner that was not temporally or spatially targeted, we used high power laser scanning of the neuroepithelium. This resulted in cell death events that were distributed throughout the tissue (8.5 ± 1.9 cell death events per animal per 30 min with 1.5 ± 0.1 PI^+ cells per cell death event, n = 10 animals). Under these conditions the calcium waves and tissue contractions were still spatially and temporally highly correlated with cell death events (Figures 2A-2K and Movie S2). Importantly, tissue contractions and cell expulsions induced by high power laser scanning occurred in the absence of any physical perturbation to the tissue, confirming that they are not a consequence of tissue disruption but are active processes triggered by the ensuing cell death events. These experiments also showed that tissue contractions and cell expulsions can be triggered by the death of just one cell (Figures 2B-2F).

In an additional set of experiments, we found that targeted induction of cell death by a high voltage electrical stimulus (2.6 ± 0.3 PI^+ cells per stimulus, n = 4 animals) resulted in calcium waves, tissue contractions and cell expulsions with kinetics that were indistinguishable from those induced by mechanical insult or high power laser scanning (Figure S2 and Movie S3).

When the tissue was exposed to low power laser scanning as during the delivery of mechanical or electrical stimuli, we did not detect cell death events or cell expulsions, and the frequency of calcium waves and tissue contractions was very low (Figures 2L-2O). Equally, we did not observe tissue contractions or cell expulsions in animals imaged using brightfield illumination (n = 8 animals). Taken together, these data confirm that cell death following wounding can trigger calcium waves, tissue contractions and cell expulsions in the developing brain.

Nuclear movement and cell shape changes parallel tissue dynamics during neuroepithelial contractions

To explore the tissue dynamics underlying apical-basal neuroepithelial contractions in more detail, we used the cell-permeant nuclear dye Hoechst 34580 to visualize cell nuclei in OGB-1 loaded animals during high power laser scanning. By tracing the nuclei of individual neuroepithelial cells over time (Figure 3A), we found that nuclei close to the origin of the calcium wave moved radially towards the center of the tissue, ‘pulling’ the ventricular and pial surfaces towards one another (Figure 3B). Cell nuclei located away from the center of the wave were displaced laterally, presumably by forces generated by the central radial contraction (Figure 3B). The distance between

nuclei close to the wave center rapidly decreased during the contraction before increasing again, with dynamics very similar to those detected in measurements of tissue thickness (Figures 3C). The reduction in distance between nuclei during tissue contraction was similar to contraction amplitude (Figure 3D).

We hypothesized that the pronounced radial contractions of the neuroepithelium would also lead to changes in progenitor cell geometry, in particular to a change in the ratio of radial to tangential extent of a cell. To investigate this, we used the cell membrane marker β-BODIPY® FL C_5-HPC (BODIPY® FL) to visualize cell membranes in the optic tectum of embryos during high-power laser scanning. This allowed us to observe changes in cell geometry during neuroepithelial contractions (Figure 3E). Consistent with a radial tissue contraction, we observed a decrease and subsequent increase in the ratio of radial to tangential cellular extent (Figures 3F and 3G). Therefore, overall tissue contractions within the neuroepithelium are closely paralleled at the cellular level.

Necrosis but not apoptosis triggers rapid cell expulsion

We were keen to establish the types of cell death that can trigger rapid cell expulsion. Apoptosis is a form of programmed cell death where cells undergo a well-defined sequence of biochemical processes including Caspase activation, which ultimately lead to a fragmentation of the cell into apoptotic bodies. Importantly, membrane integrity is preserved until late stages of apoptosis, thereby preventing the leakage of cellular contents into the

surrounding tissue. Conversely, necrotic cell death resulting from wounding does not involve Caspase activation and leads to rapid loss of membrane integrity (Kroemer et al., 2009). The fact that cells took up PI within seconds of mechanical wounding or electrical stimulation (Figures 1E-1I and S2B-S2F) confirmed that they died through necrosis rather than apoptosis. On the other hand, PI uptake during laser-induced wounding occurred at various times after the onset of high power laser scanning (Figures 2H and 2J) and could therefore represent the late phase of an apoptotic cell death program. To investigate whether cell death during laser scanning is the result of apoptotis or necrosis, we exposed control or OGB-1 loaded animals to high power laser light (Figures 4A-4D), followed by staining for the apoptosis marker Caspase 3. This showed that expelled cells did not express Caspase 3 (Figures 4E-4H), confirming they underwent necrotic cell death. The expulsion of PI^+ cells occurred at a comparable frequency in control and OGB-1 loaded animals, which indicated that OGB-1 does not mediate laser-induced cell death (Figures 4A-4D).

We next sought to determine whether apoptosis can induce cell expulsions in a manner similar to necrosis. When animals were reared in solution containing the protein synthesis inhibitor cycloheximide (CHX) for 6 h, we detected high numbers of Caspase 3^+ apoptotic cells, but close inspection of these fixed tissue samples did not reveal any Caspase 3^+ cells that had been expelled into the ventricle (Figure 4I). To further investigate whether apoptotic cell death can trigger cell expulsions, we exposed animals to CHX for different time intervals of up to 6 h. A subset of animals was fixed and stained for Caspase 3 to monitor induction of apoptosis, while another subset

that had been loaded with OGB-1 was repeatedly imaged at low laser power to detect calcium waves, tissue contractions and cell expulsions. While the number of Caspase 3^+ cells in the neuroepithelium started to increase after 3 h and was approximately 40-fold higher than control levels after 6 h of CHX exposure (Figure 4J), we did not detect any cell expulsion events or associated calcium waves and tissue contractions in either control or CHX-treated animals (Figure 4K). We conclude that cell expulsion is a mechanism that acts selectively on necrotic as opposed to apoptotic cells.

ATP signaling mediates calcium waves and calcium-dependent tissue contractions after wounding

Along with other cytosolic components, ATP is released in high concentrations into the extracellular space following necrotic cell death, and ATP can induce calcium waves in brain slices and retinal explants (Liu et al., 2010; Pearson et al., 2005; Weissman et al., 2004). To test whether ATP can trigger calcium waves and tissue contractions in the developing optic tectum, we focally delivered control solution or solution containing ATP to neuroepithelial cells *in vivo*. Whereas there was no tissue reaction to control solution (Figures 5A-5F; Movie S4), ATP induced calcium waves and tissue contractions with dynamics similar to those following necrotic cell death (Figures 5G-5L; Movie S4). In parallel experiments using brightfield illumination, ATP induced tissue contractions with dynamics indistinguishable from those in OGB-1 loaded brains during laser imaging (Figure S3; Movie S5).

Next, we were keen to demonstrate that calcium waves after wounding are mediated by ATP receptor activation, and to identify the types of ATP receptors that are involved. The ATP receptor family consists of ionotropic P2X and metabotropic P2Y receptors, with multiple subtypes in each group (Abbracchio et al., 2006; Khakh et al., 2001). Using an array of antagonists with overlapping selectivities (see Experimental Procedures for details of antagonist selectivities), the response profile we obtained was consistent with an involvement of both P2X and P2Y receptors in wound-induced calcium waves (Figure 5M). We then sought to confirm the contribution of intracellular calcium release downstream of ATP receptor activation. Calcium wave activity was reduced in the presence of both thapsigargin, which depletes intracellular calcium stores, and 2-APB, which inhibits IP_3-mediated calcium release (Figure 5N). Taken together, these results are consistent with ATP release from the site of injury and subsequent activation of P2X and P2Y receptors. This leads to calcium influx from the extracellular space and release from intracellular stores, which both contribute to wound-induced calcium waves.

Previous work has shown that ATP-mediated calcium waves can propagate through gap junctions (Liu et al., 2010; Weissman et al., 2004). We found that in the developing optic tectum, carbenoxolone (CBX) and flufenamic acid (FFA), two gap junction inhibitors, did not have an effect on calcium wave activity as calcium wave amplitude (Figure 5O). However, we did detect a strong correlation between the number of PI^+ cells after wounding and the size of calcium waves (Figure 5P). These results are consistent with a model where diffusion of ATP from the site of injury induces calcium waves.

An important question is what signaling mechanisms underlie tissue contractions in the developing brain downstream of ATP receptor activation. Calcium is a central regulator of cellular contractile processes through its activation of actomyosin. To investigate whether increases in intracellular calcium are required for tissue contractions, we focally delivered ATP to neuroepithelial cells in the presence or absence of the calcium chelator BAPTA. Calcium wave amplitude (43 ± 2% of control) and size (51 ± 5% of control), as well as tissue contraction amplitude (46 ± 2% of control) were all significantly reduced in BAPTA-treated animals (Figures 5Q and 5R), thus revealing that tissue contractions are calcium-dependent. Next, we sought to investigate whether calcium waves are sufficient to recapitulate ATP-mediated tissue contractions. Focal delivery of the calcium ionophores Ionomycin and A23187 to the neuroepithelium induced calcium transients in progenitor cells with dynamics very similar to those induced by ATP but they did not elicit tissue contractions (Figure 5S). These results indicate that calcium waves are necessary but not sufficient for neuroepithelial contractions, suggesting that ATP induces additional downstream effects that are essential for tissue contractions.

Rho kinase and actomyosin mediate contractions in the developing brain

Given that calcium alone was not sufficient to trigger tissue contractions in the developing brain, we were keen to identify the additional signaling events that lead to contractions downstream of ATP receptor activation. Small GTPases of the Rho family are major regulators of cytoskeletal organization and cellular

contractility, and P2Y receptors can activate Rho independently of calcium (Sauzeau et al., 2000; Siehler, 2009). Rho kinase is a major downstream effector of the small GTPase RhoA (Riento and Ridley, 2003), and we used the Rho kinase inhibitor Y-27632 to test whether Rho kinase is required for neuroepithelial contractions. Contraction amplitude was significantly reduced (24 ± 2% of control), whereas calcium wave amplitude (91 ± 10% of control) and size (102 ± 3% of control) were unaffected in the presence of Y-27632 (Figures 6A and 6B).

Both calcium and Rho kinase regulate myosin phosphorylation and therefore actomyosin contractility. To assess the role of myosin in neuroepithelial contractions, we used the non-muscle myosin II ATPase inhibitor blebbistatin (Straight et al., 2003) and found that contraction amplitude was significantly reduced (30 ± 5% of control), whereas calcium wave amplitude (104 ± 8% of control) and size (84 ± 13% of control) were unaffected (Figures 6C and 6D). These results strongly support a role for cytoskeletal reorganization and actomyosin contraction in neuroepithelial contractions. To directly monitor cytoskeletal dynamics during wound-induced contractions, we expressed the F-actin reporter GFP-UtrCH in the optic tectum, which is based on the actin-binding domain of Utrophin (Burkel et al., 2007). Interestingly, we observed a redistribution of actin from the apical towards the basolateral region at the site of cell expulsion (Figures 6E-6R; Movie S6). Importantly, this redistribution also occurred at a distance of at least 50 μm along the ventricular wall on either side of the injury, showing that it was not restricted to the immediate neighborhood of the wound (Figure 6S). The range of at least 100 μm over which this relocalization occurs is therefore

similar to the size of a calcium wave (see above). Actin relocalization preceded the onset of tissue contractions by 40 ± 6 s (n = 4 animals). Taken together, these results establish that calcium and Rho kinase generate tissue contractions through cytoskeletal reorganization and actomyosin contraction downstream of ATP receptor activation.

Tissue contractions drive cell expulsions from the neuroepithelium

Our data so far support a model where necrotic cell death after wounding triggers neuroepithelial contractions, which then remove the damaged cells from the tissue. To determine whether tissue contractions in fact drive necrotic cell expulsions, we investigated the effect of inhibiting contractions on the relative frequencies of the two types of cell expulsions that we observed in the developing brain. These were 'complete' cell expulsions where the entire cell was removed from the tissue, and 'incomplete' cell expulsions, where part of the cell body remained in the tissue (Figure 7A). Consistent with a model where the contraction pushes cells out of the tissue, the distance of the cell body from the ventricle prior to expulsion was related to the type of cell expulsion. In particular, the cell body of completely expelled cells was located closer to the ventricular wall (10 ± 1 μm, n = 6 animals) than that of incompletely expelled cells (18 ± 2 μm, n = 6 animals).

Importantly, we found that necrotic cells were significantly less likely to be completely expelled from the brain when the amplitude of tissue contractions was reduced with Y-27632 (Figure 7B) or blebbistatin (Figure 7C). Furthermore, both the speed of expulsion and the size of expelled cells correlated closely with contraction amplitude (Figures 7D and 7G). Both were

significantly reduced (speed, 26 ± 6% of control and size, 41 ± 6% of control) in the presence of Y-27632 (Figures 7E and 7H). Likewise, there was a significant reduction in both speed and size (speed, 56 ± 7% of control and size, 66 ± 6% of control) in blebbistatin-treated as compared to control embryos (Figures 7F and 7I). These findings demonstrate that tissue contractions drive the expulsion of necrotic cells from the neuroepithelium.

Cell expulsion prevents secondary cell death in the tissue surrounding the wound

The release of potentially toxic intracellular substances from necrotic cells after wounding can lead to damage in neighboring cells and exacerbate tissue injury. Consistent with this, PI^+ cells in the optic tectum occurred in localized clusters (Figure 8A) as confirmed by analysis of nearest neighbor distances (Figure 8B) using a bootstrap protocol ($p < 0.01$, $n = 13$ animals). We reasoned that contraction-mediated cell expulsion might be a protective mechanism to prevent the spread of tissue damage after wounding. Consistent with this, we observed few cell death events in regions of the tectum without primary necrosis (Figures 8C-8F and 8S) or regions with completely expelled necrotic cells (Figures 8G-8J and 8S). In contrast, secondary cell death frequently occurred in regions with incompletely expelled cells (Figures 8K-8R and 8S). In some cases, secondary cell death after incomplete expulsion of a primary necrotic cell could lead to the death of a field of cells spanning the entire apical-basal extent of the neuroepithelium (Figures 8O-8R). Successive cell death events around an incompletely expelled cell could trigger further calcium waves and tissue contractions, but

contraction amplitude declined as necrotic cells accumulated, presumably reflecting a decline in overall tissue integrity (Figure 8T).

Next, we were interested to see whether incompletely expelled cells with accumulated secondary necrotic cells would remain in the tissue or eventually be removed. Using long-term imaging, we found that 100%, 88%, 66%, 41%, 31% and 18% of necrotic cell clusters remained in the tissue at 0, 2, 4, 8, 24 and 48 h after injury (n = 8 animals), consistent with previous reports of slow removal of necrotic cells through passive movement or phagocytic uptake (Andrade and Rosenblatt, 2011; Sieger et al., 2012). These findings demonstrate that necrotic cells can impair tissue integrity for at least two days when they are not immediately removed from the tissue.

To further test a potential tissue protective role of contraction-mediated cell expulsions, we quantified the spread of tissue damage in animals treated with Y-27632 or blebbistatin, where the proportion of completely expelled cells is significantly reduced (Figures 7B and 7C). Importantly, we found an increase in the rate of secondary necrosis both in the presence of Y-27632 (Figure 8U) and blebbistatin (Figure 8V). This was not due to an effect of either drug on cell viability as we observed no cell death events under low-power imaging (n ≥ 4 animals). Thus, contraction-mediated cell expulsion acts to prevent the spread of tissue damage and is beneficial to wound healing through its rapid restoration of tissue integrity.

DISCUSSION

In the present study we have identified a tissue protective mechanism that acts after traumatic injury in the developing brain and is underpinned by two key observations. First, ATP release from necrotic cells after wounding triggers calcium waves, which together with Rho kinase induce cytoskeletal reorganization and actomyosin activation and thereby generate pronounced apical-basal contractions of the neuroepithelium. Second, these contractions drive the rapid and selective expulsion of necrotic cells from the tissue, which prevents the subsequent death of neighboring cells.

Surprisingly, neuroepithelial contractions occur on a timescale of seconds, which is comparable to contractions in smooth muscle. Embryonic epithelia can undergo actomyosin-dependent apical-basal contractions during developmental processes such as fruit fly morphogenetic furrow formation (Corrigall et al., 2007) and endoderm invagination in ascidians (Sherrard et al., 2010), but these processes occur on a timescale of hours, rather than seconds. Meanwhile, studies in gastrulating embryos have shown that epithelial sheets can exhibit contractile behavior on a timescale of seconds as part of normal morphogenetic processes such as convergent extension (Wallingford et al., 2001). This raises the interesting possibility that an actomyosin-dependent contractile mechanism used in early morphogenesis may be reused later in development as part of the wound healing process. The fact that tissue contractions persist until at least four months of age indicates that this or similar mechanisms can also operate in more mature tissues, potentially even in adulthood.

Our observations of actomyosin-mediated cell expulsions after tissue injury extend the role of actomyosin activation in embryonic wound healing.

Previous work has shown that one of the earliest events in the healing of embryonic skin wounds is the assembly of a multicellular actomyosin 'purse string' at the wound edge (Bement et al., 1993; Martin and Lewis, 1992; McCluskey and Martin, 1995). Similar contractile actomyosin cables also act to close single-cell wounds (Bement et al., 1999) and to extrude apoptotic cells from epithelial monolayers (Andrade and Rosenblatt, 2011; Gu et al., 2011; Rosenblatt et al., 2001). The assembly of the actomyosin purse string after skin wounding is regulated by Rho GTPases (Benink and Bement, 2005; Clark et al., 2009; Soto et al., 2013). The rapid timescale of signaling events immediately after wounding suggests that transcription-independent events such as tension changes around the wound or intercellular signaling through material released from the injured cells could mediate an elevation in intracellular calcium and cytoskeletal remodeling (Clark et al., 2009; Cordeiro and Jacinto, 2013; Joshi et al., 2010). Our results show that ATP release from necrotic cells can trigger calcium waves, and that reorganization of the actin cytoskeleton precedes neuroepithelial contractions. This reorganization involves a flow of actin from the apical to the basolateral domain of neuroepithelial cells. Consistent with this, pulsed flow of actomyosin away from apical junctions is required for cellular contraction in fruit fly gastrulation (Martin et al., 2009) and germband extension (Rauzi et al., 2010). Conversely, we did not find evidence for the formation of contractile actomyosin cables around necrotic cells during expulsion. This is consistent with previous reports that apoptotic but not necrotic cells assemble actomyosin rings (Andrade and Rosenblatt, 2011).

Wound-induced calcium waves act to recruit phagocytes to the site of injury in the developing brain (Sieger et al., 2012), and calcium waves can increase proliferation of neural progenitor cells (Weissman et al., 2004), which could compensate for cell loss resulting from traumatic injury. ATP-mediated calcium waves therefore emerge as central players in coordinating the response of the developing brain to wounding.

Despite its clinical significance (Baethmann et al., 1996; Hayes et al., 2007; Leroy-Malherbe et al., 2006), the process of wound healing in the developing brain is only beginning to be understood. Scarless wound healing occurs in the retina (Halfter, 1993) and midbrain (Lawson and England, 1992; 1996) of the early chick embryo, but how this is accomplished on a molecular and cellular level has remained elusive. Immediately after wounding, cells that die as a result of the injury lose membrane integrity, and cytosolic contents are released into the local tissue environment. Some cellular components such as degradative enzymes and reactive oxygen species can cause damage to the surrounding tissue and thereby directly aggravate the primary injury. In addition, the release of intracellular components initiates an inflammatory response and serves to recruit phagocytes to the wound site, which take up cellular debris and contain invading pathogens. While initially beneficial, excessive inflammation can slow the healing process and further exacerbate the primary wound (Martin and Leibovich, 2005; Novo and Parola, 2008). The tissue protective mechanism that we have described achieves removal of necrotic cells from the tissue within seconds of wounding. This is several orders of magnitude faster than previously reported mechanisms such as phagocytic uptake of necrotic cells (Krysko et al., 2006). By virtue of its

speed, rapid cell expulsion prevents the spread of secondary cell death and therefore represents a tissue-level mechanism that is well placed to mediated fast wound healing with minimal inflammation and scarring in the developing brain.

EXPERIMENTAL PROCEDURES

Animals

Wild-type *Xenopus laevis* tadpoles were reared on a 14 h light/10 h dark cycle at 15-21 °C in Modified Barth's Solution (MBS, 87.6 mM NaCl, 1 mM KCl, 2.3 mM $NaHCO_3$, 14.9 mM HEPES, 0.3 mM $CaNO_3$, 0.8 mM $MgSO_4$, 0.6 mM $CaCl_2$, 10 U/ml Penicillin, 10 µg/ml Streptomycin, pH 7.6). Reagents were supplied by Sigma unless otherwise stated. To inhibit melanogenesis, the rearing solution also contained 100 µM N-Phenylthiourea. Tadpoles were staged according to established morphological criteria (Nieuwkoop and Faber, 1994), and experiments were conducted between stages 44 and 50. Prior to imaging, animals were anaesthetized by immersion in MBS containing 0.01% Ethyl 3-aminobenzoate methansulfonate (MS-222). For imaging brain explants, tadpoles were euthanized in 2% MS-222 immediately before removal of the brain and the explants were imaged in artificial cerebrospinal fluid (ACSF, 115 mM NaCl, 2 mM KCl, 5 mM HEPES, 0.01 mM glycine, 10 mM D-glucose, 3 mM $CaCl_2$, 1.5 mM $MgCl_2$, pH 7.2). All animal procedures were conducted in accordance with UK Home Office regulations.

Progenitor cell labeling

To visualize the morphology of individual progenitor cells and their progeny, we used single cell electroporation of fluorescent dextran. See Supplemental Experimental Procedures for details.

In vivo live cell imaging

Live imaging of calcium in the optic tectum was carried out using Oregon Green BAPTA-1 AM (OGB-1 AM, Invitrogen). See Supplemental Experimental Procedures for details.

For visualization of necrotic cell death, cell nuclei or cell membranes, 100 µg/ml PI (Invitrogen), 1 mg/ml Hoechst 34580 (Invitrogen) or 100 µg/ml β-BODIPY® FL C_5-HPC (Invitrogen) in calcium-free Ringer's solution with 0.03% Fast Green were injected into the tectal ventricle. For quantification of necrotic cell death after mechanical injury (see below for details), z stacks with 5 µm intervals between optical planes and spanning the entire depth of the optic tectum were taken after wounding and the number of PI^+ cells was counted manually.

Imaging was conducted on a custom-built multiphoton microscope equipped with a MaiTai-HP Ti:Sapphire femtosecond pulsed laser (Newport Spectra-Physics), a ×40 0.8 NA LUMPlanFI/IR objective (Olympus) and Fluoview FV300 image acquisition software (Olympus). The laser was operated at 910 nm, and images from individual animals were acquired at 1 s, 2 s or 5 s intervals for up to 30 min. Laser power at the sample was 5-8 mW during imaging except when laser scanning was used to induce wounding (see below for details).

Brightfield imaging was conducted on an Olympus BX51WI upright microscope equipped with a ×40 0.8 NA LUMPlanFI/IR objective (Olympus), a DMK 41BU02 CCD camera (The Imaging Source) and IC Capture image acquisition software (The Imaging Source). Images from individual animals were acquired at 5 s intervals for up to 30 min.

In vitro transcription and microinjection of mRNA

For visualization of F-actin dynamics, we obtained a plasmid encoding the F-actin reporter GFP-UtrCH in pCS2+ (Addgene plasmid 26737) from which mRNA was transcribed *in vitro* using the mMessage mMachine SP6 kit (Ambion). A total amount of 1 ng mRNA was injected into one-cell stage embryos and mRNA expression in the optic tectum was assessed at the desired developmental stage.

Induction of cell necrosis

To induce targeted cell death by mechanical injury, a fine glass micropipette was positioned 10 µm from the ventricular wall, rapidly moved 30 µm in the direction of the ventricular wall, and then returned to its original position. To induce targeted cell death by electrical stimulation, our single-cell electroporation protocol was modified to deliver focal high voltage pulses (amplitude of 20 V) to progenitor cells lining the wall of the ventricle. To induce cell death in a manner that was not temporally or spatially targeted, we used high power laser scanning in which the multiphoton laser was set to achieve 25-40 mW at the sample, and was scanned repeatedly across the entire field of view. This resulted in cell death events that could be initiated anywhere within the tissue.

Drug treatments

Pharmacological agents for manipulation of signaling pathways in the optic tectum were injected into the tectal neuropil or the brain ventricle. See Supplemental Experimental Procedures for details.

Immunohistochemistry

We used rabbit anti-Caspase 3 antibody (BD Pharmingen) to detect apoptotic cells in the optic tectum. See Supplemental Experimental Procedures for details.

Image processing and analysis

Fluorescence and brightfield images were acquired as uncompressed bitmaps in BMP or TIFF format, and figures were assembled in Adobe Illustrator CS6. Quantitative analysis of calcium signaling, tissue contractions, movements of cell nuclei, changes in cell geometry, cell expulsions and actin dynamics was carried out in ImageJ (http://rsbweb.nih.gov/ij) and MATLAB (Mathworks). See Supplemental Experimental Procedures for details.

Statistical methods

All population data are presented as mean ± sem. Statistical analysis was performed using Prism (GraphPad Software). Briefly, data sets were assessed for normality and appropriate statistical tests were carried out as stated in the figure legends. For analysis of spatial distribution of PI^+ cells (Figure 8B), we used a bootstrap analysis in MATLAB. See Supplemental Experimental Procedures for details.

SUPPLEMENTAL INFORMATION

Supplemental Information includes Supplemental Experimental Procedures, three figures and six movies.

ACKNOWLEDGEMENTS

We would like to thank Gero Miesenböck, Andrew Oates, Antony Galione, Grant Churchill, and members of the Akerman lab for helpful discussions and comments on the manuscript. We are grateful to Andrew Oates and Philip Pinheiro for help with mRNA transcription. This work was supported by grants from the Biotechnology and Biological Sciences Research Council (BB/E0154761), and the research leading to these results has received funding from the European Research Council under the European Community's Seventh Framework Programme (FP7/2007-2013), ERC grant agreement number 243273. L.H. was supported by a European Blaschko Visiting Research Fellowship and an EMBO Long-Term Fellowship.

REFERENCES

Abbracchio, M.P., Burnstock, G., Boeynaems, J.-M., Barnard, E.A., Boyer, J.L., Kennedy, C., Knight, G.E., Fumagalli, M., Gachet, C., Jacobson, K.A., et al. (2006). International Union of Pharmacology LVIII: update on the P2Y G protein-coupled nucleotide receptors: from molecular mechanisms and pathophysiology to therapy. Pharmacol. Rev. *58*, 281–341.

Andrade, D., and Rosenblatt, J. (2011). Apoptotic regulation of epithelial cellular extrusion. Apoptosis *16*, 491–501.

Baethmann, M., Kahn, T., Lenard, H.G., and Voit, T. (1996). Fetal CNS damage after exposure to maternal trauma during pregnancy. Acta Paediatr. *85*, 1331–1338.

Bement, W.M., Forscher, P., and Mooseker, M.S. (1993). A novel cytoskeletal structure involved in purse string wound closure and cell polarity maintenance. J. Cell Biol. *121*, 565–578.

Bement, W.M., Mandato, C.A., and Kirsch, M.N. (1999). Wound-induced assembly and closure of an actomyosin purse string in Xenopus oocytes. Curr. Biol. *9*, 579–587.

Benink, H.A., and Bement, W.M. (2005). Concentric zones of active RhoA and Cdc42 around single cell wounds. J. Cell Biol. *168*, 429–439.

Bielefeld, K.A., Amini-Nik, S., and Alman, B.A. (2013). Cutaneous wound

healing: recruiting developmental pathways for regeneration. Cell. Mol. Life Sci. *70*, 2059–2081.

Burkel, B.M., Dassow, von, G., and Bement, W.M. (2007). Versatile fluorescent probes for actin filaments based on the actin-binding domain of utrophin. Cell Motil. Cytoskeleton *64*, 822–832.

Clark, A.G., Miller, A.L., Vaughan, E., Yu, H.-Y.E., Penkert, R., and Bement, W.M. (2009). Integration of single and multicellular wound responses. Curr. Biol. *19*, 1389–1395.

Cordeiro, J.V., and Jacinto, A. (2013). The role of transcription-independent damage signals in the initiation of epithelial wound healing. Nat. Rev. Mol. Cell Biol. *14*, 249–262.

Corrigall, D., Walther, R.F., Rodriguez, L., Fichelson, P., and Pichaud, F. (2007). Hedgehog signaling is a principal inducer of Myosin-II-driven cell ingression in Drosophila epithelia. Dev. Cell *13*, 730–742.

Crosby, L.M., and Waters, C.M. (2010). Epithelial repair mechanisms in the lung. Am. J. Physiol. Lung Cell Mol. Physiol. *298*, L715–L731.

Degen, K.E., and Gourdie, R.G. (2012). Embryonic wound healing: a primer for engineering novel therapies for tissue repair. Birth Defects Res. C Embryo Today *96*, 258–270.

Gu, Y., Forostyan, T., Sabbadini, R., and Rosenblatt, J. (2011). Epithelial cell extrusion requires the sphingosine-1-phosphate receptor 2 pathway. J. Cell

Biol. *193*, 667–676.

Gurtner, G.C., Werner, S., Barrandon, Y., and Longaker, M.T. (2008). Wound repair and regeneration. Nature *453*, 314–321.

Halfter, W. (1993). Effect of wound healing and tissue transplantation on the navigation of axons in organ-cultured embryonic chick eyes. J. Comp. Neurol. *327*, 442–457.

Hayes, B., Ryan, S., Stephenson, J.B.P., and King, M.D. (2007). Cerebral palsy after maternal trauma in pregnancy. Dev Med Child Neurol *49*, 700–706.

Joshi, S.D., Dassow, von, M., and Davidson, L.A. (2010). Experimental control of excitable embryonic tissues: three stimuli induce rapid epithelial contraction. Exp. Cell Res. *316*, 103–114.

Khakh, B.S., Burnstock, G., Kennedy, C., King, B.F., North, R.A., Séguéla, P., Voigt, M., and Humphrey, P.P. (2001). International union of pharmacology. XXIV. Current status of the nomenclature and properties of P2X receptors and their subunits. Pharmacol. Rev. *53*, 107–118.

Kroemer, G., Galluzzi, L., Vandenabeele, P., Abrams, J., Alnemri, E.S., Baehrecke, E.H., Blagosklonny, M.V., El-Deiry, W.S., Golstein, P., Green, D.R., et al. (2009). Classification of cell death: recommendations of the Nomenclature Committee on Cell Death 2009. Cell Death Differ. *16*, 3–11.

Krysko, D.V., D'Herde, K., and Vandenabeele, P. (2006). Clearance of apoptotic and necrotic cells and its immunological consequences. Apoptosis *11*, 1709–1726.

Larson, B.J., Longaker, M.T., and Lorenz, H.P. (2010). Scarless fetal wound healing: a basic science review. Plast. Reconstr. Surg. *126*, 1172–1180.

Lawson, A., and England, M.A. (1992). Studies on wound healing in the neuroepithelium of the chick embryo. Anat. Rec. *233*, 291–300.

Lawson, A., and England, M.A. (1996). The effect of embryonic cerebrospinal fluid pressure and morphogenetic brain expansion on wound healing in the midbrain of the chick embryo. Anat. Embryol. *193*, 601–610.

Lázár, G. (1973). The development of the optic tectum in Xenopus laevis: a Golgi study. J. Anat. *116*, 347–355.

Leroy-Malherbe, V., Bonnier, C., Papiernik, E., Groos, E., and Landrieu, P. (2006). The association between developmental handicaps and traumatic brain injury during pregnancy: an issue that deserves more systematic evaluation. Brain Inj *20*, 1355–1365.

Liu, X., Hashimoto-Torii, K., Torii, M., Ding, C., and Rakic, P. (2010). Gap junctions/hemichannels modulate interkinetic nuclear migration in the forebrain precursors. J. Neurosci. *30*, 4197–4209.

Lo, D.D., Zimmermann, A.S., Nauta, A., Longaker, M.T., and Lorenz, H.P. (2012). Scarless fetal skin wound healing update. Birth Defects Res. C Embryo Today *96*, 237–247.

Martin, A.C., Kaschube, M., and Wieschaus, E.F. (2009). Pulsed contractions of an actin-myosin network drive apical constriction. Nature *457*, 495–499.

Martin, P., and Lewis, J. (1992). Actin cables and epidermal movement in embryonic wound healing. Nature *360*, 179–183.

Martin, P., and Leibovich, S.J. (2005). Inflammatory cells during wound repair: the good, the bad and the ugly. Trends Cell Biol. *15*, 599–607.

McCluskey, J., and Martin, P. (1995). Analysis of the tissue movements of embryonic wound healing--DiI studies in the limb bud stage mouse embryo. Dev. Biol. *170*, 102–114.

Naik-Mathuria, B., Gay, A.N., Zhu, X., Yu, L., Cass, D.L., and Olutoye, O.O. (2007). Age-dependent recruitment of neutrophils by fetal endothelial cells: implications in scarless wound healing. J. Pediatr. Surg. *42*, 166–171.

Nieuwkoop, P.D., and Faber, J. (1994). Normal Table of Xenopus laevis (Daudin). Garland Publishing, New York.

Novo, E., and Parola, M. (2008). Redox mechanisms in hepatic chronic wound healing and fibrogenesis. Fibrogenesis Tissue Repair *1*, 5.

Pearson, R.A., Dale, N., Llaudet, E., and Mobbs, P. (2005). ATP released via gap junction hemichannels from the pigment epithelium regulates neural retinal progenitor proliferation. Neuron *46*, 731–744.

Rauzi, M., Lenne, P.-F., and Lecuit, T. (2010). Planar polarized actomyosin

contractile flows control epithelial junction remodelling. Nature *468*, 1110–1114.

Razzell, W., Evans, I.R., Martin, P., and Wood, W. (2013). Calcium flashes orchestrate the wound inflammatory response through DUOX activation and hydrogen peroxide release. Curr. Biol. *23*, 424–429.

Riento, K., and Ridley, A.J. (2003). Rocks: multifunctional kinases in cell behaviour. Nat. Rev. Mol. Cell Biol. *4*, 446–456.

Rosenblatt, J., Raff, M.C., and Cramer, L.P. (2001). An epithelial cell destined for apoptosis signals its neighbors to extrude it by an actin- and myosin-dependent mechanism. Curr. Biol. *11*, 1847–1857.

Sauer, F.C. (1935). Mitosis in the neural tube. J. Comp. Neurol. *62*, 377–405.

Sauzeau, V., Le Jeune, H., Cario-Toumaniantz, C., Vaillant, N., Gadeau, A.P., Desgranges, C., Scalbert, E., Chardin, P., Pacaud, P., and Loirand, G. (2000). P2Y(1), P2Y(2), P2Y(4), and P2Y(6) receptors are coupled to Rho and Rho kinase activation in vascular myocytes. Am. J. Physiol. Heart Circ. Physiol. *278*, H1751–H1761.

Sherrard, K., Robin, F., Lemaire, P., and Munro, E. (2010). Sequential activation of apical and basolateral contractility drives ascidian endoderm invagination. Curr. Biol. *20*, 1499–1510.

Sieger, D., Moritz, C., Ziegenhals, T., Prykhozhij, S., and Peri, F. (2012). Long-range Ca2+ waves transmit brain-damage signals to microglia. Dev.

Cell *22*, 1138–1148.

Siehler, S. (2009). Regulation of RhoGEF proteins by G12/13-coupled receptors. Br. J. Pharmacol. *158*, 41–49.

Singer, A.J., and Clark, R.A. (1999). Cutaneous wound healing. N. Engl. J. Med. *341*, 738–746.

Sonnemann, K.J., and Bement, W.M. (2011). Wound repair: toward understanding and integration of single-cell and multicellular wound responses. Annu. Rev. Cell Dev. Biol. *27*, 237–263.

Soto, X., Li, J., Lea, R., Dubaissi, E., Papalopulu, N., and Amaya, E. (2013). Inositol kinase and its product accelerate wound healing by modulating calcium levels, Rho GTPases, and F-actin assembly. Proc. Natl. Acad. Sci. U.S.a. *110*, 11029–11034.

Straight, A.F., Cheung, A., Limouze, J., Chen, I., Westwood, N.J., Sellers, J.R., and Mitchison, T.J. (2003). Dissecting temporal and spatial control of cytokinesis with a myosin II Inhibitor. Science *299*, 1743–1747.

Straznicky, K., and Gaze, R.M. (1972). The development of the tectum in Xenopus laevis: an autoradiographic study. J Embryol Exp Morphol *28*, 87–115.

Wallingford, J.B., Ewald, A.J., Harland, R.M., and Fraser, S.E. (2001). Calcium signaling during convergent extension in Xenopus. Curr. Biol. *11*, 652–661.

Weissman, T.A., Riquelme, P.A., Ivic, L., Flint, A.C., and Kriegstein, A.R. (2004). Calcium waves propagate through radial glial cells and modulate proliferation in the developing neocortex. Neuron *43*, 647–661.

Whitby, D.J., Longaker, M.T., Harrison, M.R., Adzick, N.S., and Ferguson, M.W. (1991). Rapid epithelialisation of fetal wounds is associated with the early deposition of tenascin. J. Cell. Sci. *99 (Pt 3)*, 583–586.

FIGURE LEGENDS

Figure 1. Cell death after wounding induces calcium waves and tissue contractions in the developing brain, and damaged cells are expelled into the ventricle

(A) Head of a stage 48 *Xenopus laevis*. FB, forebrain. MB, midbrain. HB, hindbrain. OT, optic tectum. Scale bar represents 200 μm.

(B) The posterior-lateral region of the optic tectum is comprised of a neuroepithelium. The dashed line represents the border between neurons and neural progenitors. NPs, neural progenitors. P, pia. V, ventricle. Scale bar represents 10 μm.

(C) Radial neural progenitors (asterisk) and a migrating neuron (arrowhead) labeled by single-cell electroporation. The panel is a composite of three images of individual progenitors, as indicated by the dotted lines. Scale bar represents 10 μm.

(D) The optic tectum was loaded with the calcium indicator OGB-1 and an average of ten time frames is shown for an overview of tissue architecture. The radial line indicates where epithelial thickness was measured and the circle represents the area where calcium fluorescence was measured. Scale bar represents 10 μm.

(E-I) Time series of the optic tectum loaded with OGB-1 and PI. A cell that dies following mechanical injury (arrow) is expelled into the ventricle during neuroepithelial contraction. Solid white lines represent tissue outline at t = 0 s and dashed white lines represent tissue outline at the specified time.

(J) Quantification of calcium transient, tissue contraction and cell expulsion. The arrow indicates the timing of cell death through mechanical injury. ET, epithelial thickness. EA, expelled area.

(K) Inducing cell death via a range of different stimuli leads to coincident calcium waves, tissue contractions and cell expulsions. n ≥ 4 animals in each condition.

See also Figure S1 and Movie S1.

Figure 2. Inducing necrotic cell death via high power laser scanning leads to calcium waves, tissue contractions and cell expulsions

(A) The optic tectum was loaded with the calcium indicator OGB-1 and an average of ten time frames is shown for an overview of tissue architecture. The radial line indicates where epithelial thickness was measured and the circle represents the area where calcium fluorescence was measured. Scale bar represents 10 μm.

(B-F) Time series of the optic tectum loaded with OGB-1 and PI. High power laser scanning leads to the death of a tectal cell (arrow) which is associated with a calcium wave and tissue contraction. The dead cell is then expelled into the ventricle. There is an additional calcium wave that originates slightly posterior to the location of the cell death event, leading to a small calcium transient around 150 s. Some individual cells also display calcium transients independently of calcium waves. Solid white lines represent tissue outline at t-= 0 s and dashed white lines represent tissue outline at the specified time.

(G) Quantification of calcium transient, tissue contraction, and cell expulsion. The arrow indicates the timing of cell death through high-power laser scanning. ET, epithelial thickness. EA, expelled area.

(H-K) Correlations of time and location of cell death events with time and location of calcium wave onset or tissue contraction onset. n = 6 animals in each condition. r, Pearson's correlation coefficient.

(L-O) Quantification of cell death events, calcium waves, tissue contractions and cell expulsions with low power or high power laser scanning. n = 10 animals in each condition. ** $p < 0.01$ in Mann-Whitney U test.

All population data are represented as mean ± sem.

See also Figure S2 and Movies S2 and S3.

Figure 3. Neuroepithelial contractions are associated with relative movement of cell nuclei and changes in cell shape

(A) The optic tectum was loaded with the calcium indicator OGB-1 and the nuclei of tectal cells were stained with Hoechst. Even though both calcium and Hoechst fluorescence were recorded, only Hoechst is shown for clarity. The centers of nuclei labeled in blue were traced during tissue contraction. White solid lines represent tissue outline at t = 0 s, and magenta dashed lines at t = 60 s. The white dotted line indicates an expelled cell. Scale bar represents 10 μm.

(B) The movement of individual nuclei between t = 0 s and t = 60 s is represented by blue arrows. The green star shows the location of calcium wave onset.

(C) The blue traces show the distance between six pairs of nuclei centered around the location of calcium wave onset. Pairs of nuclei were radially aligned, with one close to the ventricular surface and one close to the pial surface. The magenta trace shows epithelial thickness measured at the location of calcium wave onset. The arrow indicates the timing of cell death through high power laser scanning.

(D) The reduction in distance between nuclei during tissue contractions is similar to contraction amplitude. n = 44 cells in 5 animals.

(E) The optic tectum was loaded with the cell membrane marker BODIPY® FL and PI. Even though both BODIPY® FL and PI fluorescence were recorded, only BODIPY® FL is shown for clarity. The length and width of colored cells, defined as their radial and tangential extent, were measured during tissue contraction. White solid lines represent tissue outline at t = 0 s, and white dashed lines at t = 60 s. The white punctate line indicates an expelled cell. Scale bar represents 10 μm.

(F) The colored traces show the ratio of cell length to width during a tissue contraction. The black trace shows epithelial thickness measured at the location of cell death. The arrow indicates the timing of cell death through high power laser scanning.

(G) The ratio of cell length to width is consistently reduced during tissue contractions. ** $p < 0.01$ in Mann-Whitney U test. n = 56 cells in 4 animals.

All population data are represented as mean ± sem.

Figure 4. Necrotic but not apoptotic cell death triggers cell expulsion

(A-C) Live images of the optic tectum loaded with PI (A,B) or OGB-1 and PI (C). Arrows indicate expelled cells. Scale bar represents 10 μm.

(D) Quantification of cell expulsion. n ≥ 16 animals in each condition. ** $p < 0.01$ in Kruskal-Wallis test with Dunn's post test.

(E-G) The optic tectum fixed and stained for Caspase 3 and cell nuclei. Arrows indicate expelled cells. Scale bar represents 10 μm.

(H) Quantification of Caspase 3^+ cells. n ≥ 8 animals in each condition. No significant differences were detected in Kruskal-Wallis test with Dunn's post test.

(I) The optic tectum fixed and stained for Caspase 3 and cell nuclei after 6 h of CHX exposure. Scale bar represents 10 μm.

(J) Time course of Caspase 3 activation in control and CHX-treated animals. n ≥ 2 animals in each condition. * $p < 0.05$ and ** $p < 0.01$ in Kruskal-Wallis test with Dunn's post test.

(K) Expulsion events in control and CHX-treated animals. n = 5 animals in each condition.

All population data are represented as mean ± sem.

Figure 5. ATP signaling mediates calcium waves and tissue contractions after wounding

(A-E) and (G-K) The optic tectum was loaded with OGB-1 and a puff of ACSF (A-E) or ATP in ACSF (G-K) was delivered onto the ventricular wall at t = 0 s. The radial line indicates where epithelial thickness was measured and the circle represents the area where calcium fluorescence was measured. Solid

white lines represent tissue outline at t = 0 s and dashed white lines represent tissue outline at the specified time. Scale bar represents 10 μm.

(F,L) Quantification of calcium transient and tissue contraction from (A-E) and (G-K). Arrows indicate the timing of puffs. ET, epithelial thickness.

(M) Quantification of calcium wave activity after mechanical injury in the presence of different ATP receptor antagonists. n ≥ 6 animals in each condition. * $p < 0.05$ and ** $p < 0.01$ in Kruskal-Wallis test with Dunn's post test.

(N) Quantification of calcium wave activity after ATP puffs in the presence of different inhibitors of intracellular calcium release. n ≥ 6 animals in each condition. * $p < 0.05$ and ** $p < 0.01$ in Kruskal-Wallis test with Dunn's post test.

(O) Quantification of calcium wave activity after ATP puffs in the presence of different gap junction inhibitors. n ≥ 6 animals in each condition. No significant differences were detected in Kruskal-Wallis test with Dunn's post test.

(P) Correlation of injury size with calcium wave size. n = 18 animals. r, Pearson's correlation coefficient.

(Q) Calcium transients and tissue contractions in response to ATP in a control animal and an animal treated with the calcium chelator BAPTA. Arrows indicate the timing of puffs.

(R) Calcium wave amplitude, number of cells in a calcium wave and tissue contraction amplitude are all reduced in BAPTA-treated animals. n ≥ 4 animals in each condition. ** $p < 0.01$ in Mann-Whitney U test.

(S) Calcium transients and tissue contractions in response to focal application of the calcium ionophores Ionomycin and A23187. Arrows indicate the timing of puffs.

All population data are represented as mean ± sem.

See also Figure S3 and Movies S4 and S5.

Figure 6. Tissue contractions in the developing neuroepithelium are mediated by Rho kinase and actomyosin, and preceded by a reorganization of the actin cytoskeleton

(A) Calcium transients and tissue contractions in response to ATP in a control animal and an animal treated with the Rho kinase inhibitor Y-27632. Arrows indicate the timing of puffs. ET, epithelial thickness.

(B) Contraction amplitude, but not calcium wave amplitude or number of cells in a calcium wave, are reduced in Y27632-treated animals. $n \geq 6$ animals in each condition. ** $p < 0.01$ in Mann-Whitney U test.

(C) Calcium transients and tissue contractions in a control animal and an animal treated with the non-muscle myosin II ATPase inhibitor blebbistatin. Arrows indicate the timing of cell death through high power laser scanning.

(D) Contraction amplitude, but not calcium wave amplitude or number of cells in a calcium wave, are reduced in blebbistatin-treated animals. $n \geq 23$ animals in each condition. ** $p < 0.01$ in Mann-Whitney U test.

(E) The F-actin reporter GFP-UtrCH was expressed in the optic tectum and an average of ten time frames is shown for an overview of tissue architecture. Scale bar represents 10 μm.

(F-P) Time series of the area of the optic tectum indicated in (E) expressing GFP-UtrCH and injected with PI. The boxes indicate where fluorescence was measured at the expulsion site. High power laser scanning induces a cell death event (arrow), reorganization of the actin cytoskeleton, and tissue contraction. Solid white lines represent tissue outline at t = 0 s and dashed white lines represent tissue outline at the specified time. Scale bar represents 10 μm.

(Q) Quantification of GFP-UtrCH fluorescence and tissue contraction. Preceding the tissue contraction, F-actin relocalizes from the apical towards the basolateral region of the neuroepithelium. The blue and orange traces show GFP-UtrCH fluorescence in the boxes indicated in (F). The black trace shows epithelial thickness measured at the location of cell death. Arrow indicates timing of cell death through high power laser scanning.

(R) Relocalization of GFP-UtrCH fluorescence from the apical towards the basolateral region occurs at the site of cell expulsion. Region 1 spans the area between 0 and 2 μm from the ventricular surface, and Region 2 spans the area between 2 and 10 μm from the ventricular surface. In both regions, fluorescence was measured in a box with a lateral extent of 20 μm centered on the location of cell death. n = 4 animals. * $p < 0.05$ in Wilcoxon Signed Rank Test.

(S) Relocalization of GFP-UtrCH fluorescence also occurs at a distance of 50 μm from the cell expulsion. Fluorescence in Regions 1 and 2 was measured in two boxes, each with a lateral extent of 20 μm. These were centered on positions at a distance of 50 μm along the ventricular wall on

either side of the location of cell death. n = 4 animals. ** $p < 0.01$ in Wilcoxon Signed Rank Test.

All population data are represented as mean ± sem.

See also Movie S6.

Figure 7. Tissue contractions are required for successful cell expulsions from the neuroepithelium after wounding

(A) Complete cell expulsion, where the entire cell body of one cell is removed from the tissue (upper panel) and incomplete cell expulsion, where part of the cell body remains in the tissue (lower panel). Scale bar represents 10 μm.

(B,C) Blocking tissue contractions with Y-27632 (B) or blebbistatin (C) reduces the proportion of complete cell expulsions. CE, complete expulsion. IE, incomplete expulsion. n ≥ 8 animals (B) and n ≥ 23 animals (C) in each condition.* $p < 0.05$ in Fisher's exact test.

(D,G) Correlation of contraction amplitude with expulsion speed (D) and size (G). n = 23 animals. r, Pearson's correlation coefficient.

(E,H) Expulsion speed (E) and size (H) are reduced in the presence of Y-27632. n ≥ 8 animals in each condition. ** $p < 0.01$ in Student's t test.

(F,I) Expulsion speed (F) and size (I) are reduced in the presence of blebbistatin. n ≥ 23 animals in each condition. ** $p < 0.01$ in Student's t test.

All population data are represented as mean ± sem.

Figure 8. The rapid expulsion of necrotic cells reduces secondary cell death after wounding in the developing brain

(A) Clusters of PI^+ cells in the optic tectum. Individual PI^+ cell are labeled by an asterisk. Scale bar represents 10 μm.

(B) The mean nearest neighbor distance between PI^+ cells in (A), as indicated by the dashed line, is shorter than predicted by chance using a bootstrap protocol (gray histogram).

(C-F) An area of the optic tectum without primary necrotic cells. Scale bar represents 10 μm.

(G-J) An area of the optic tectum with a completely expelled necrotic cell. No further cell death events were observed.

(K-N) An area of the optic tectum with an incompletely expelled cell. A cell neighboring the primary necrotic cell also undergoes cell death (asterisk).

(O-R) An area of the optic tectum with two incompletely expelled cells. Ten neighboring cells also die (asterisk).

(S) The number of necrotic cells within two cell diameters of a completely expelled cell is the same as at randomly chosen locations without primary necrosis, but is increased near incompletely expelled cells. n = 10 animals in each condition. ** $p < 0.01$ in Kruskal-Wallis test with Dunn's post test.

(T) The amplitude of contractions triggered by successive cell death events decreases in locations with severe secondary cell death. Measurements were taken from an animal with mild (K-N) and severe (O-R) secondary cell death.

(U,V) The rate of secondary necrosis is increased when cell expulsions are blocked with Y-27632 (U) or blebbistatin (V). $n \geq 8$ animals (U) and $n \geq 23$ animals (V) in each condition. * $p < 0.05$ and ** $p < 0.01$ in Mann-Whitney U test.

All population data are represented as mean ± sem.

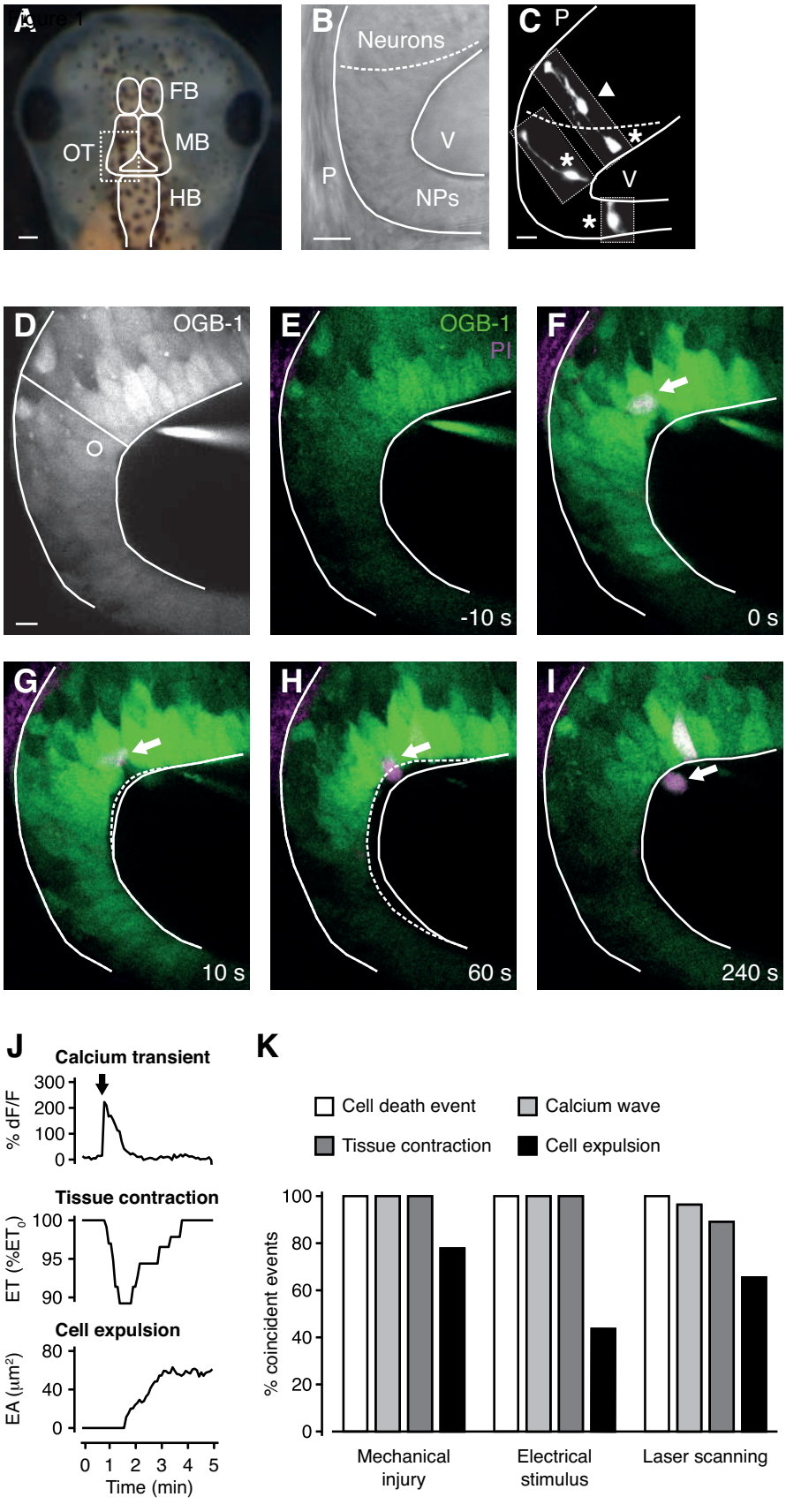
A
FB
MB
OT
HB
B
Neurons
V
P
NPs
C
P
V
D
OGB-1
O
E
OGB-1
PI
-10 s
F
0 s
G
10 s
H
60 s
I
240 s
J
Calcium transient
% dF/F
300
200
100
0
Tissue contraction
ET (%ET0)
100
95
90
Cell expulsion
EA (µm2)
80
40
0
0 1 2 3 4 5
Time (min)
K
Cell death event
Calcium wave
Tissue contraction
Cell expulsion
% coincident events
100
80
60
40
20
0
Mechanical injury
Electrical stimulus
Laser scanning

Figure 2

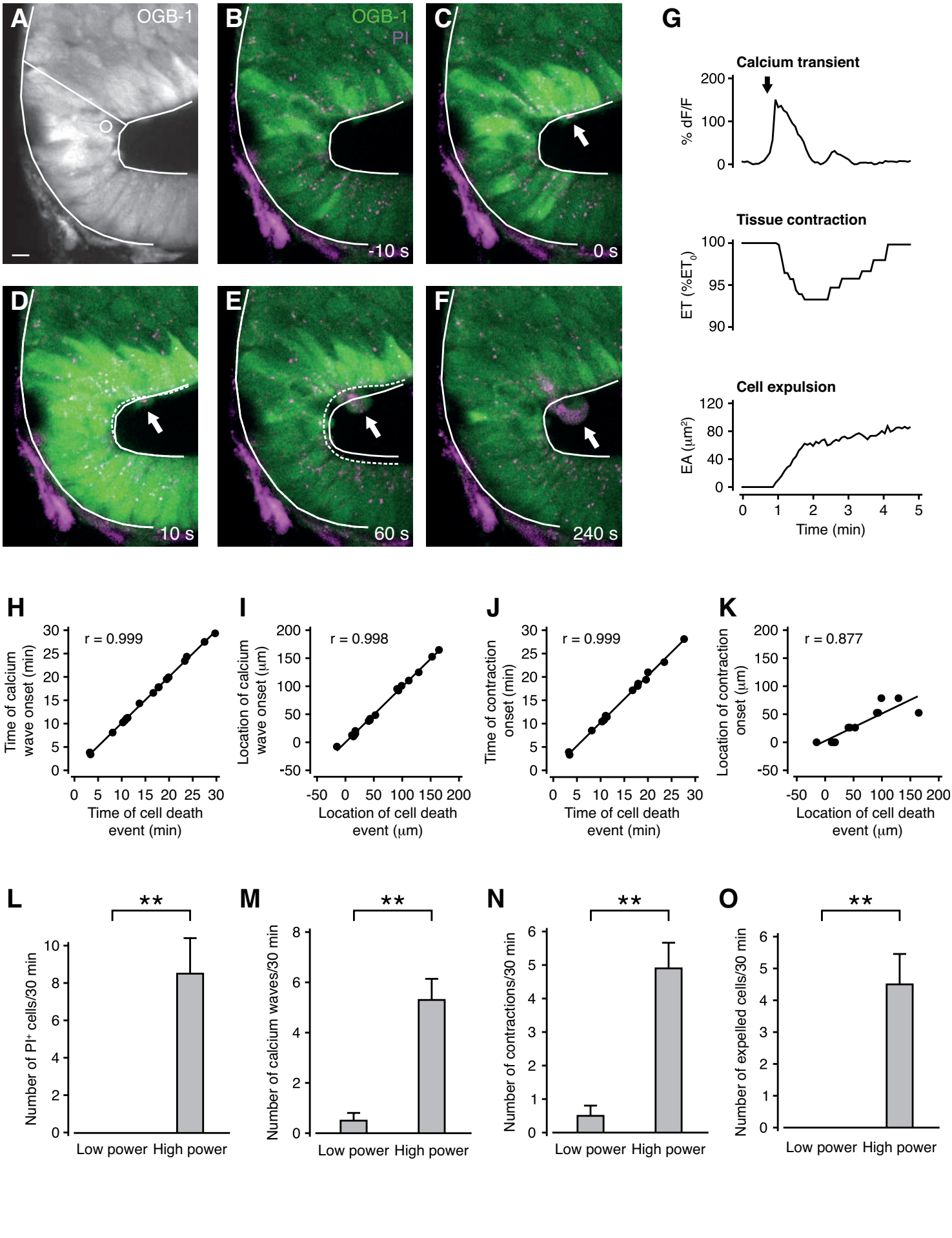
A
OGB-1
B
OGB-1
PI
-10 s
C
0 s
D
10 s
E
60 s
F
240 s
G
Calcium transient
% dF/F
Tissue contraction
ET (%ET0)
Cell expulsion
EA (μm²)
Time (min)
H
r = 0.999
Time of calcium wave onset (min)
Time of cell death event (min)
I
r = 0.998
Location of calcium wave onset (μm)
Location of cell death event (μm)
J
r = 0.999
Time of contraction onset (min)
Time of cell death event (min)
K
r = 0.877
Location of contraction onset (μm)
Location of cell death event (μm)
L
Number of PI+ cells/30 min
Low power
High power
M
Number of calcium waves/30 min
N
Number of contractions/30 min
O
Number of expelled cells/30 min

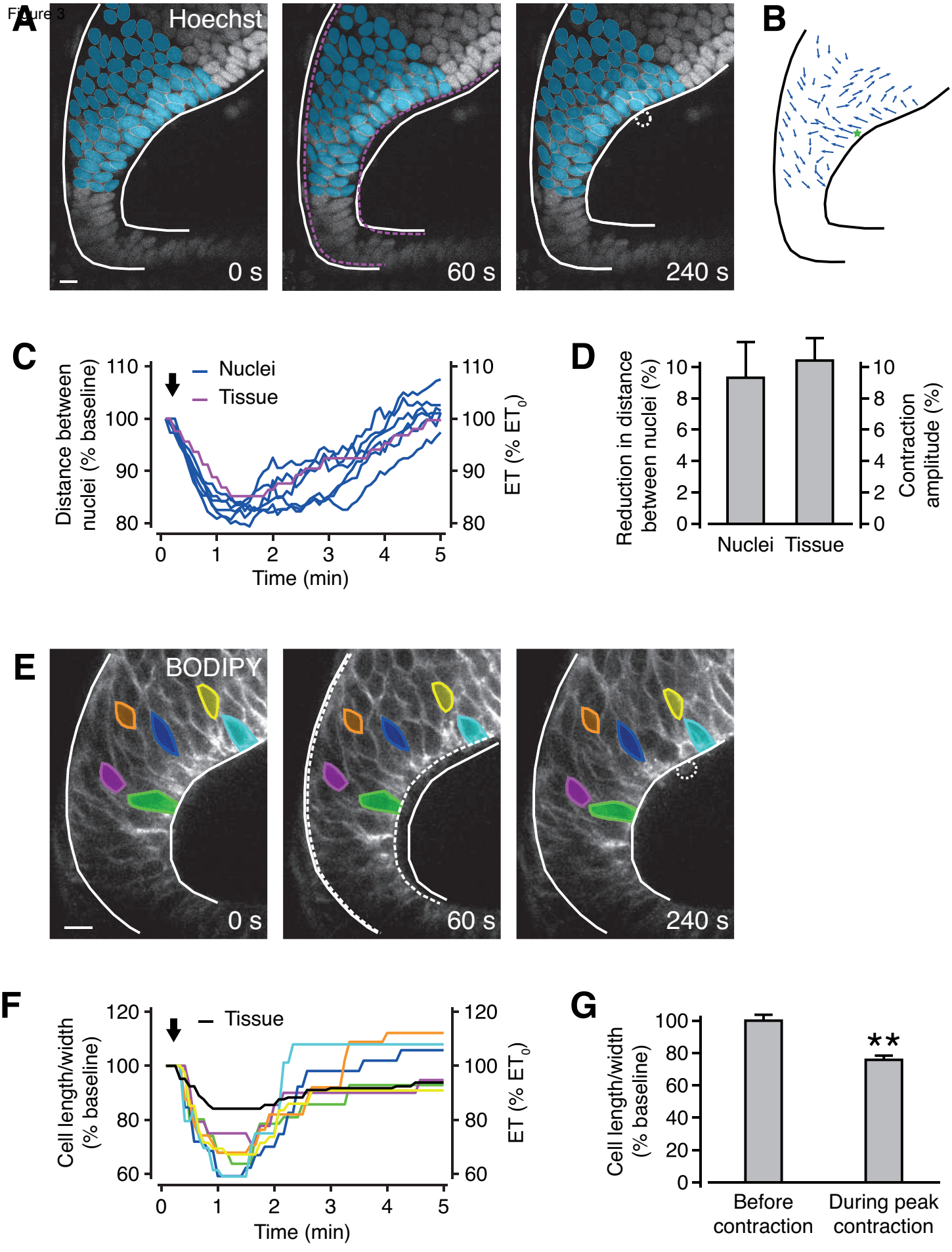
A
Hoechst
0 s
60 s
240 s
B
C
Distance between nuclei (% baseline)
Nuclei
Tissue
ET (% ET0)
Time (min)
D
Reduction in distance between nuclei (%)
Contraction amplitude (%)
Nuclei
Tissue
E
BODIPY
0 s
60 s
240 s
F
Cell length/width (% baseline)
Tissue
ET (% ET0)
Time (min)
G
Cell length/width (% baseline)
**
Before contraction
During peak contraction

Figure 4

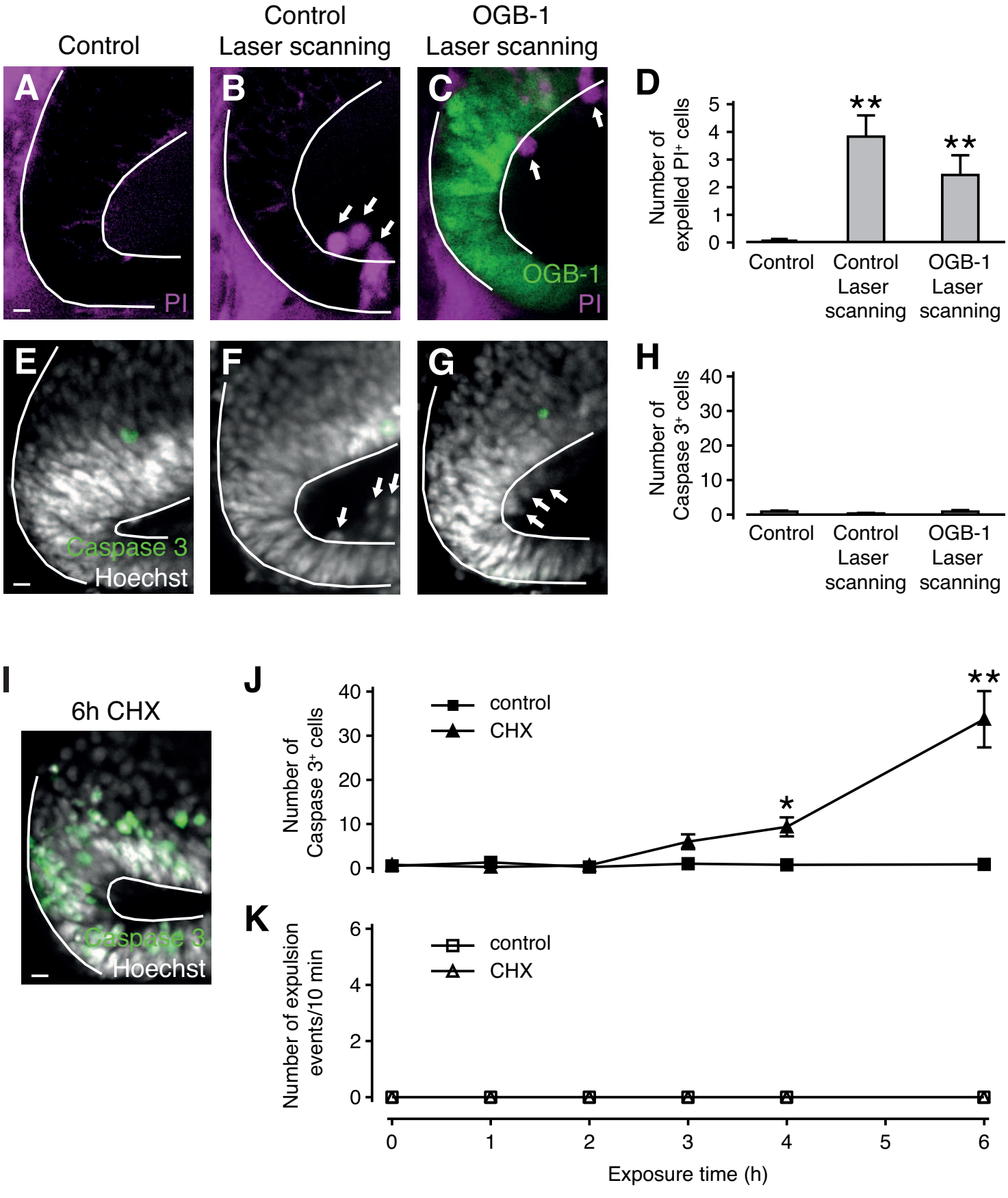
Control
Control
Laser scanning
OGB-1
Laser scanning
A
B
C
PI
OGB-1
PI
D
Number of
expelled PI+ cells
5
4
3
2
1
0
**
**
Control
Control
Laser
scanning
OGB-1
Laser
scanning
E
F
G
Caspase 3
Hoechst
H
Number of
Caspase 3+ cells
40
30
20
10
0
Control
Control
Laser
scanning
OGB-1
Laser
scanning
I
6h CHX
Caspase 3
Hoechst
J
Number of
Caspase 3+ cells
40
30
20
10
0
control
CHX
*
**
K
Number of expulsion
events/10 min
6
4
2
0
control
CHX
0
1
2
3
4
5
6
Exposure time (h)

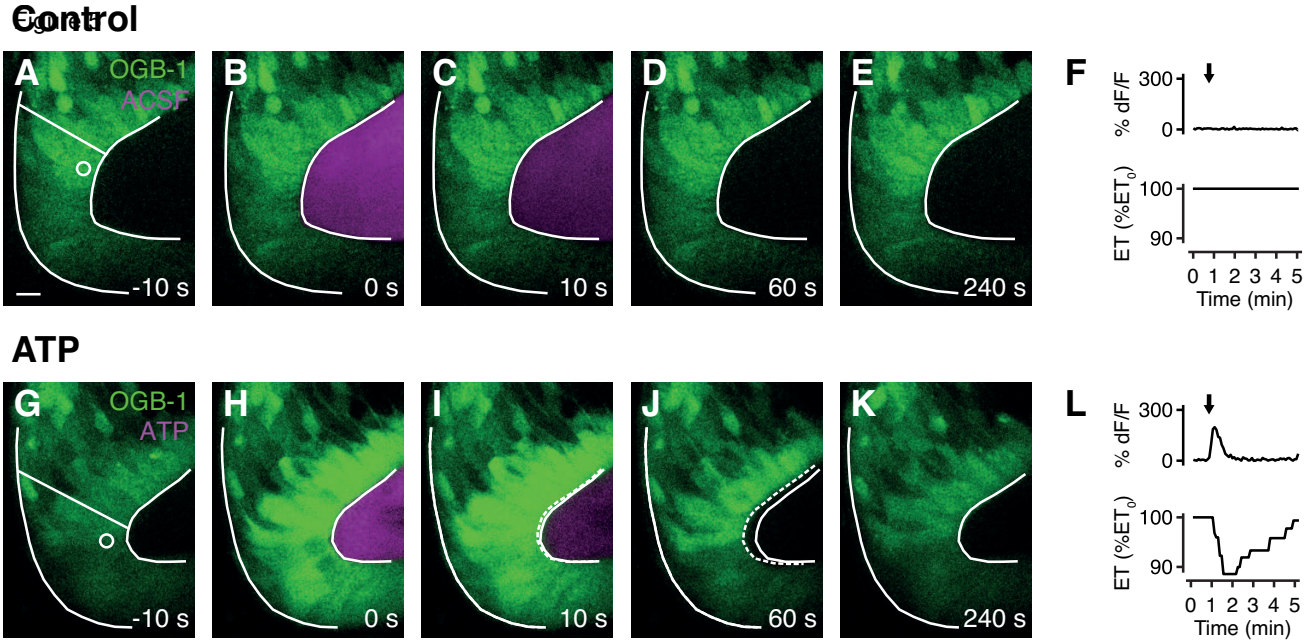
Control
A
OGB-1
ACSF
-10 s
B
0 s
C
10 s
D
60 s
E
240 s
F
% dF/F
300
0
ET (%ET0)
100
90
0 1 2 3 4 5
Time (min)
ATP
G
OGB-1
ATP
-10 s
H
0 s
I
10 s
J
60 s
K
240 s
L
% dF/F
300
0
ET (%ET0)
100
90
0 1 2 3 4 5
Time (min)

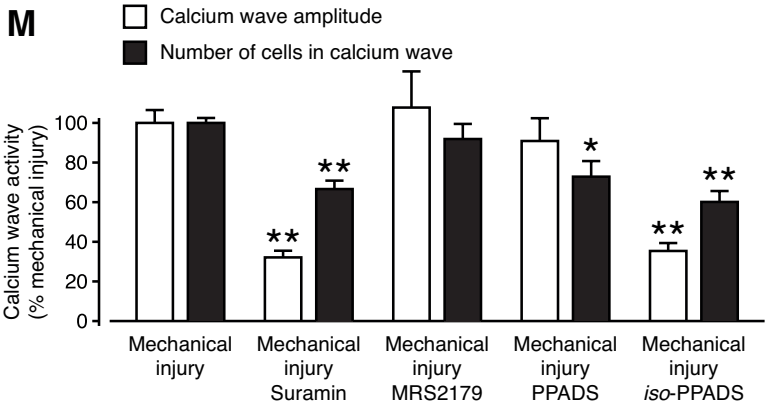
M
Calcium wave amplitude
Number of cells in calcium wave
Calcium wave activity
(% mechanical injury)
100
80
60
40
20
0
**
**
*
**
**
Mechanical injury
Mechanical injury Suramin
Mechanical injury MRS2179
Mechanical injury PPADS
Mechanical injury iso-PPADS

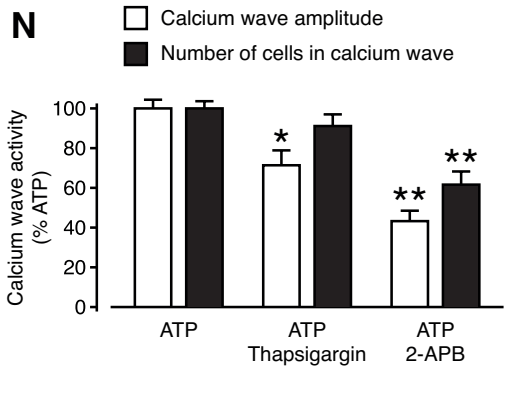
N
Calcium wave amplitude
Number of cells in calcium wave
Calcium wave activity
(% ATP)
100
80
60
40
20
0
*
**
**
ATP
ATP Thapsigargin
ATP 2-APB

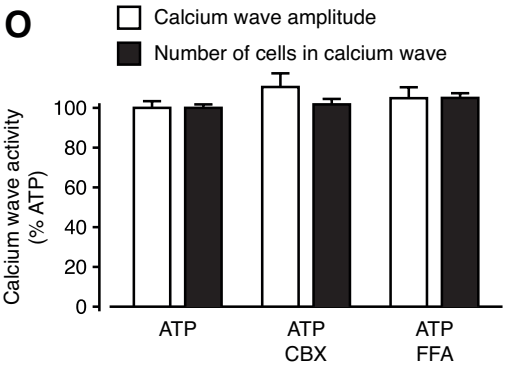
O
Calcium wave amplitude
Number of cells in calcium wave
Calcium wave activity
(% ATP)
100
80
60
40
20
0
ATP
ATP CBX
ATP FFA

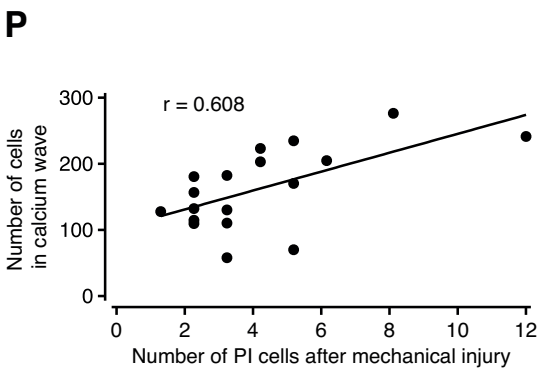
P
r = 0.608
Number of cells in calcium wave
300
200
100
0
0 2 4 6 8 10 12
Number of PI cells after mechanical injury

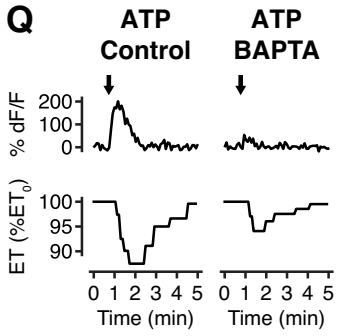
Q
ATP Control
ATP BAPTA
% dF/F
200
100
0
ET (%ET0)
100
95
90
0 1 2 3 4 5
Time (min)
0 1 2 3 4 5
Time (min)

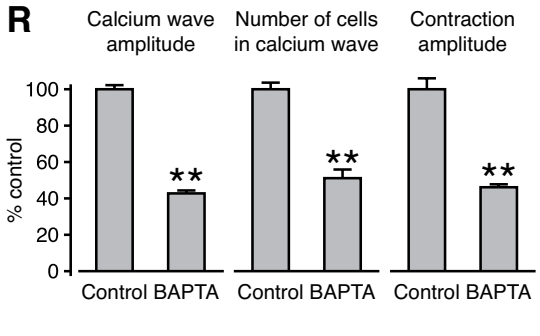
R
Calcium wave amplitude
Number of cells in calcium wave
Contraction amplitude
% control
100
80
60
40
20
0
**
**
**
Control BAPTA
Control BAPTA
Control BAPTA

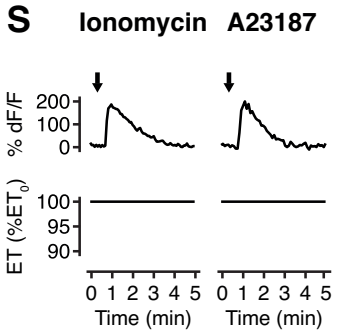
S
Ionomycin
A23187
% dF/F
200
100
0
ET (%ET0)
100
95
90
0 1 2 3 4 5
Time (min)
0 1 2 3 4 5
Time (min)

Figure 6

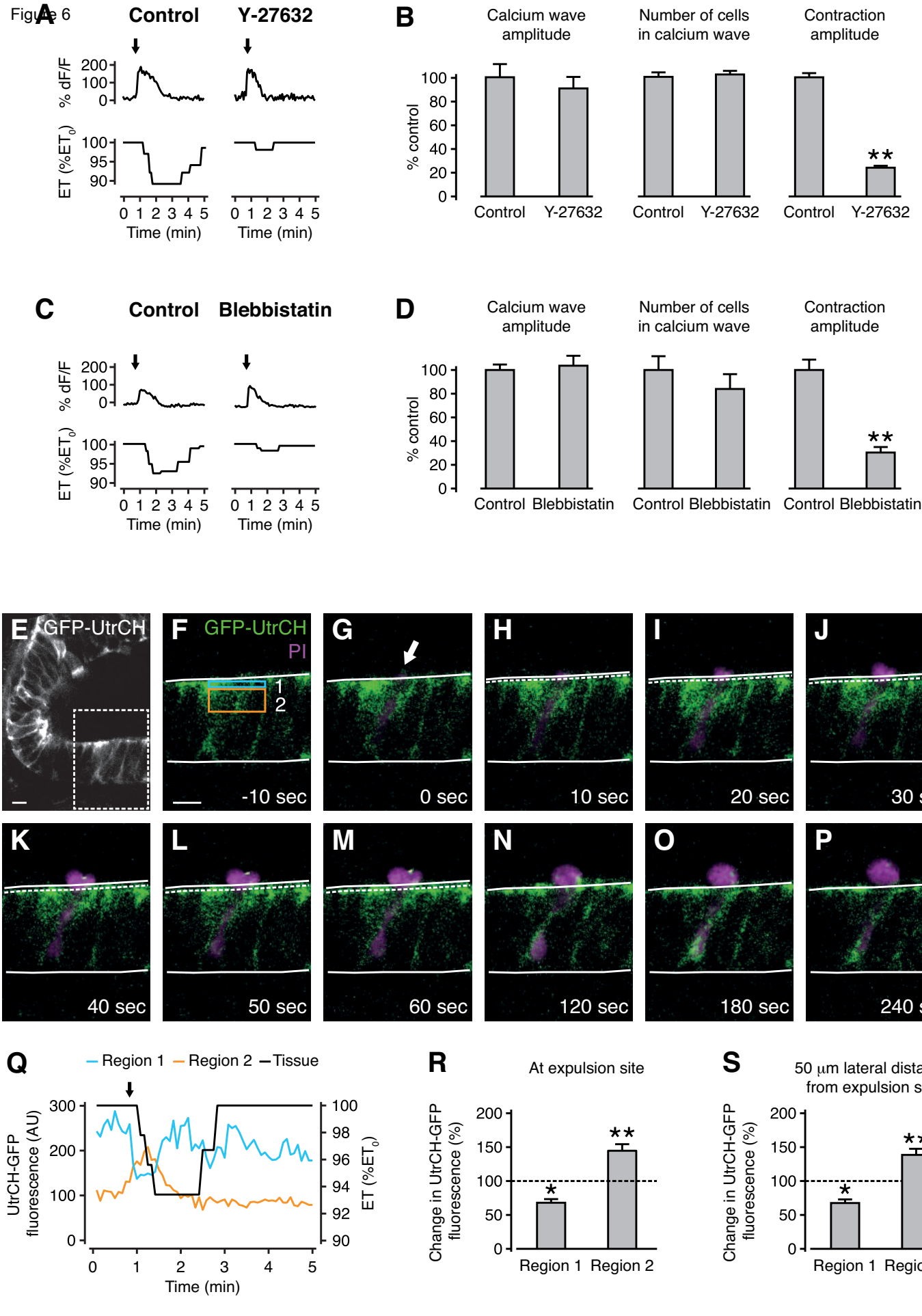
A
Control
Y-27632
% dF/F
ET (%ET0)
Time (min)
B
Calcium wave amplitude
Number of cells in calcium wave
Contraction amplitude
% control
Control
Y-27632
C
Control
Blebbistatin
D
Calcium wave amplitude
Number of cells in calcium wave
Contraction amplitude
% control
Control
Blebbistatin
E GFP-UtrCH
F GFP-UtrCH
PI
1
2
-10 sec
G
0 sec
H
10 sec
I
20 sec
J
30 sec
K
40 sec
L
50 sec
M
60 sec
N
120 sec
O
180 sec
P
240 sec
Q
Region 1
Region 2
Tissue
UtrCH-GFP fluorescence (AU)
ET (%ET0)
Time (min)
R
At expulsion site
Change in UtrCH-GFP fluorescence (%)
Region 1
Region 2
S
50 μm lateral distance from expulsion site
Change in UtrCH-GFP fluorescence (%)
Region 1
Region 2

Figure 7

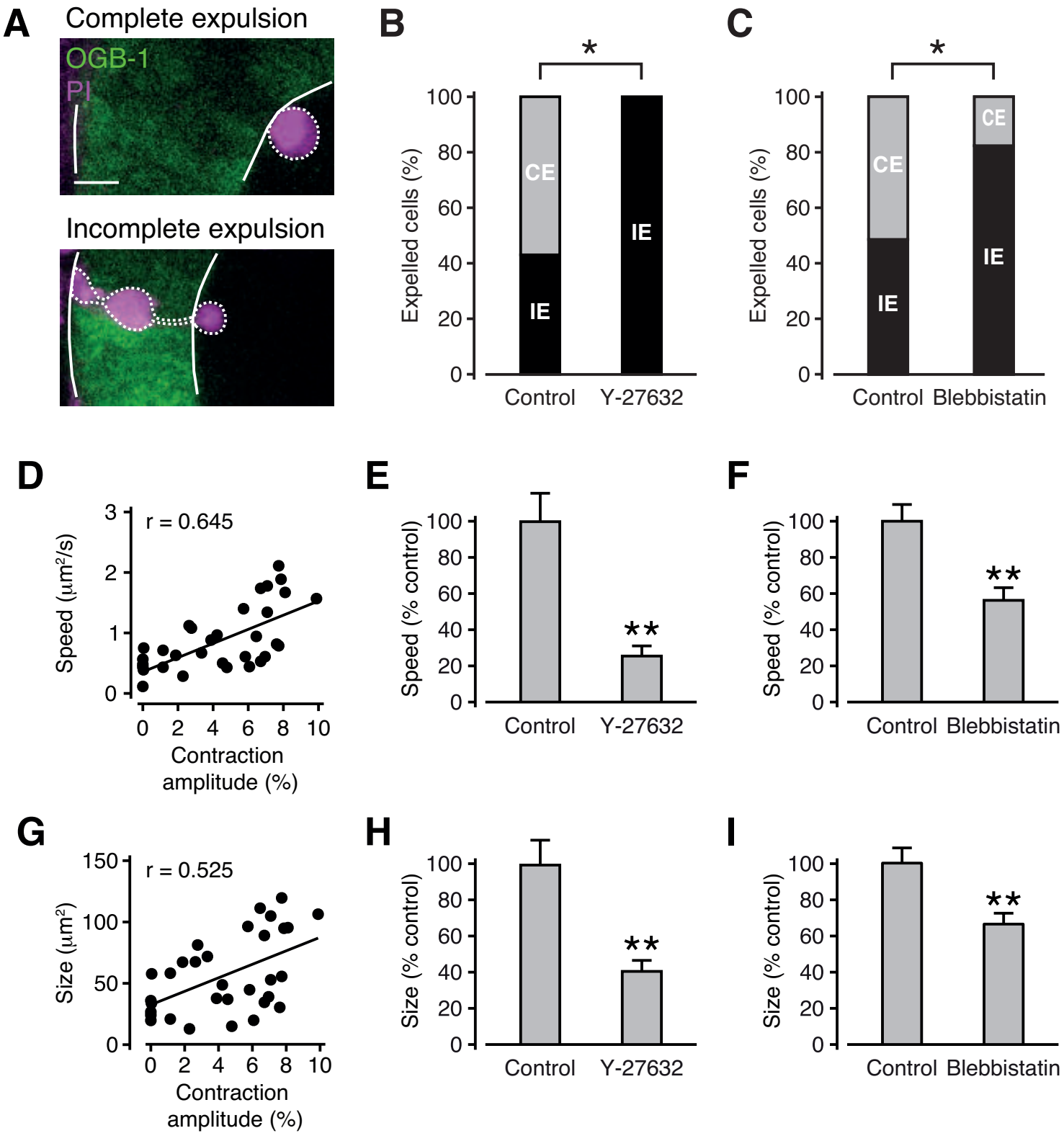
A
Complete expulsion
OGB-1
PI
Incomplete expulsion
B
*
Expelled cells (%)
100
80
60
40
20
0
CE
IE
IE
Control
Y-27632
C
*
Expelled cells (%)
100
80
60
40
20
0
CE
IE
CE
IE
Control
Blebbistatin
D
r = 0.645
Speed (μm²/s)
3
2
1
0
0 2 4 6 8 10
Contraction amplitude (%)
E
Speed (% control)
100
80
60
40
20
0
**
Control
Y-27632
F
Speed (% control)
100
80
60
40
20
0
**
Control
Blebbistatin
G
r = 0.525
Size (μm²)
150
100
50
0
0 2 4 6 8 10
Contraction amplitude (%)
H
Size (% control)
100
80
60
40
20
0
**
Control
Y-27632
I
Size (% control)
100
80
60
40
20
0
**
Control
Blebbistatin

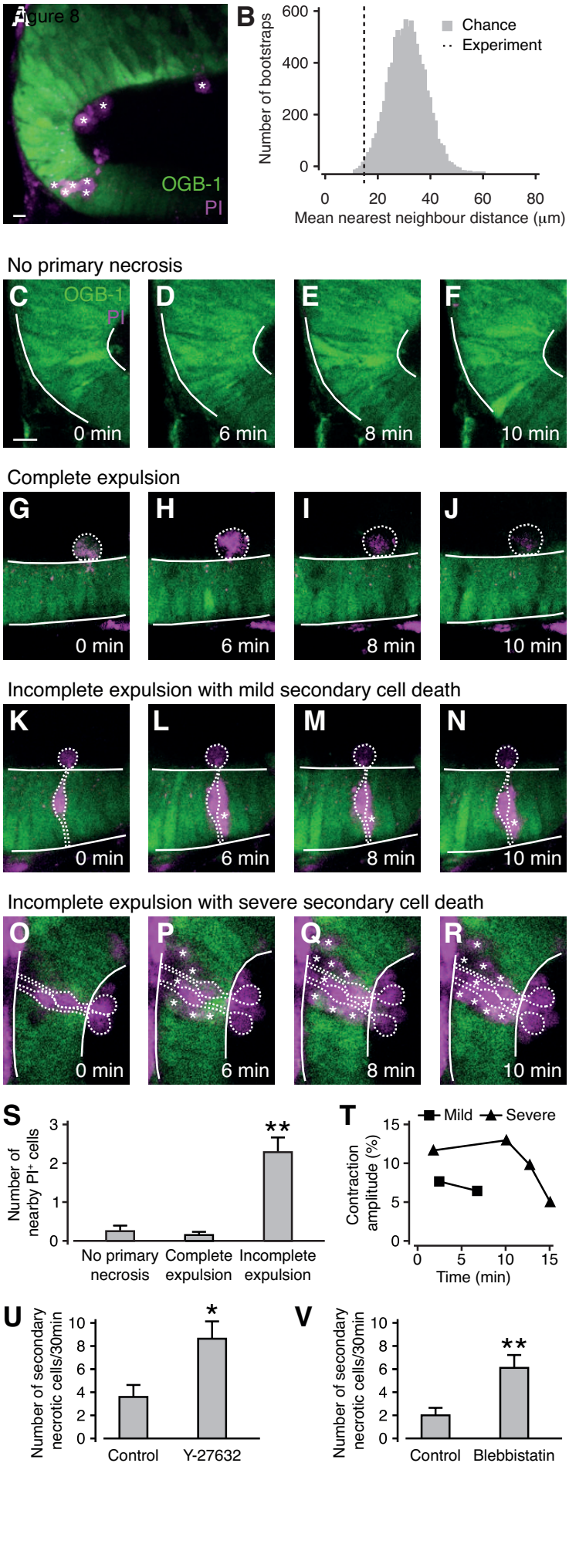
Figure 8
A
OGB-1
PI
B
Number of bootstraps
600
400
200
0
Chance
Experiment
0
20
40
60
80
Mean nearest neighbour distance (μm)
No primary necrosis
C
OGB-1
PI
0 min
D
6 min
E
8 min
F
10 min
Complete expulsion
G
0 min
H
6 min
I
8 min
J
10 min
Incomplete expulsion with mild secondary cell death
K
0 min
L
6 min
M
8 min
N
10 min
Incomplete expulsion with severe secondary cell death
O
0 min
P
6 min
Q
8 min
R
10 min
S
Number of nearby PI+ cells
3
2
1
0
**
No primary necrosis
Complete expulsion
Incomplete expulsion
T
Mild
Severe
Contraction amplitude (%)
15
10
5
0
0
5
10
15
Time (min)
U
Number of secondary necrotic cells/30min
10
8
6
4
2
0
*
Control
Y-27632
V
Number of secondary necrotic cells/30min
10
8
6
4
2
0
**
Control
Blebbistatin

SUPPLEMENTAL INVENTORY

Supplemental Figures and Figure legends

Supplemental Movies and Movie legends

Supplemental Experimental Procedures

Supplemental References

Figure S1

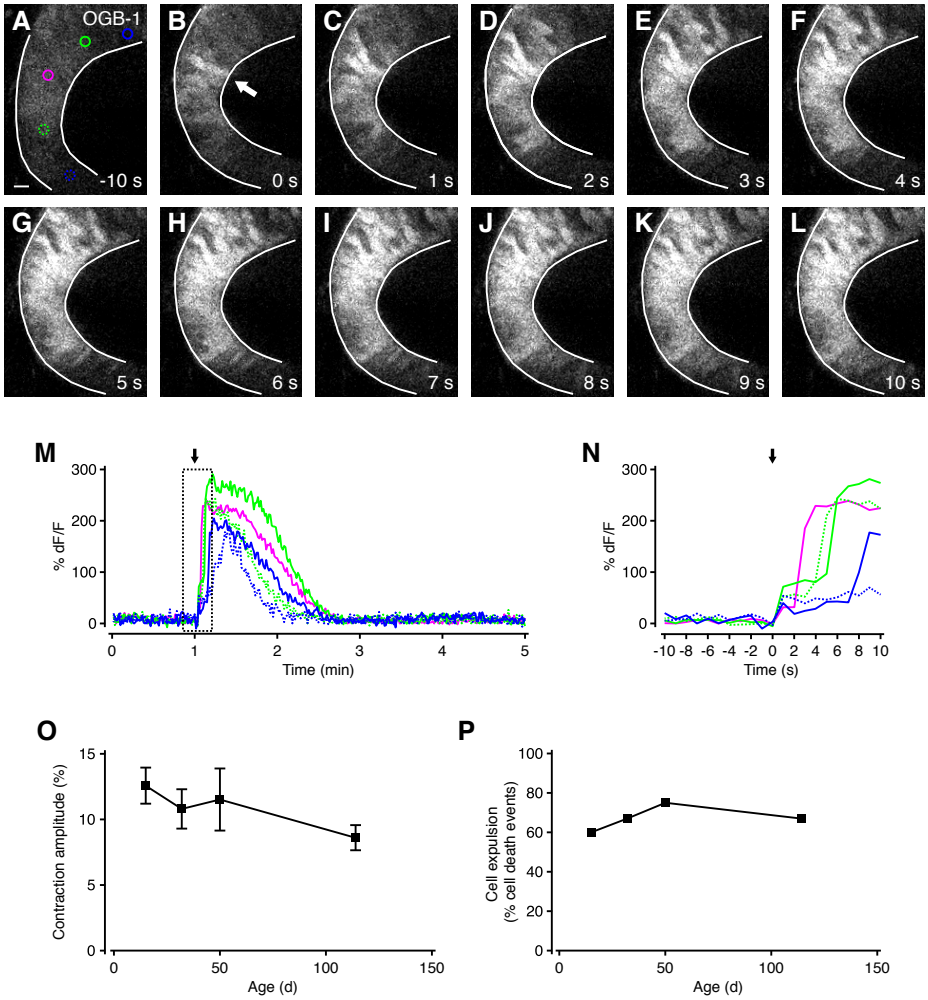
A
OGB-1
-10 s
B
0 s
C
1 s
D
2 s
E
3 s
F
4 s
G
5 s
H
6 s
I
7 s
J
8 s
K
9 s
L
10 s
M
% dF/F
Time (min)
N
% dF/F
Time (s)
O
Contraction amplitude (%)
Age (d)
P
Cell expulsion
(% cell death events)
Age (d)

Figure S2

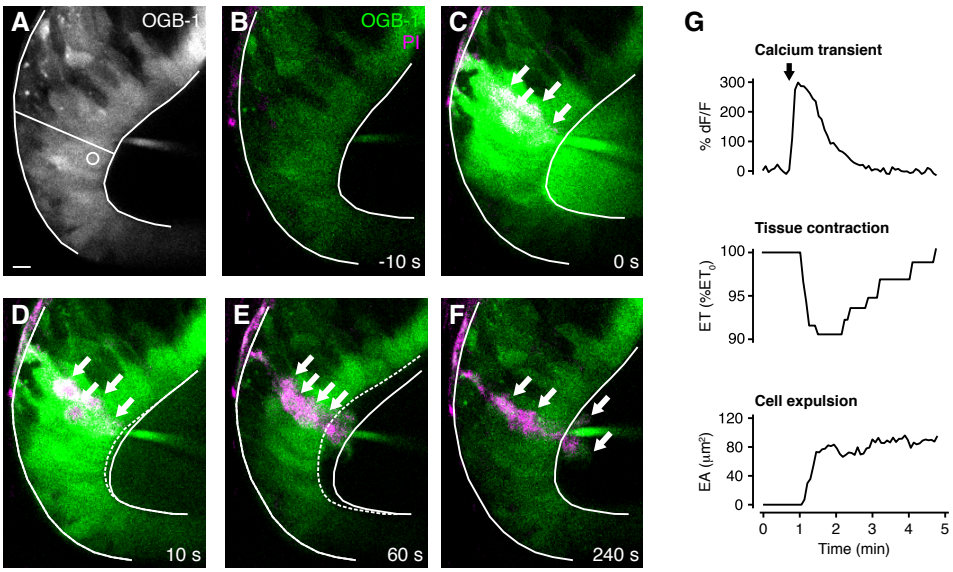
A
OGB-1
O
B
OGB-1
PI
-10 s
C
0 s
D
10 s
E
60 s
F
240 s
G
Calcium transient
% dF/F
300
200
100
0
Tissue contraction
ET (%ET0)
100
95
90
Cell expulsion
EA (µm²)
120
80
40
0
0 1 2 3 4 5
Time (min)

Figure S3

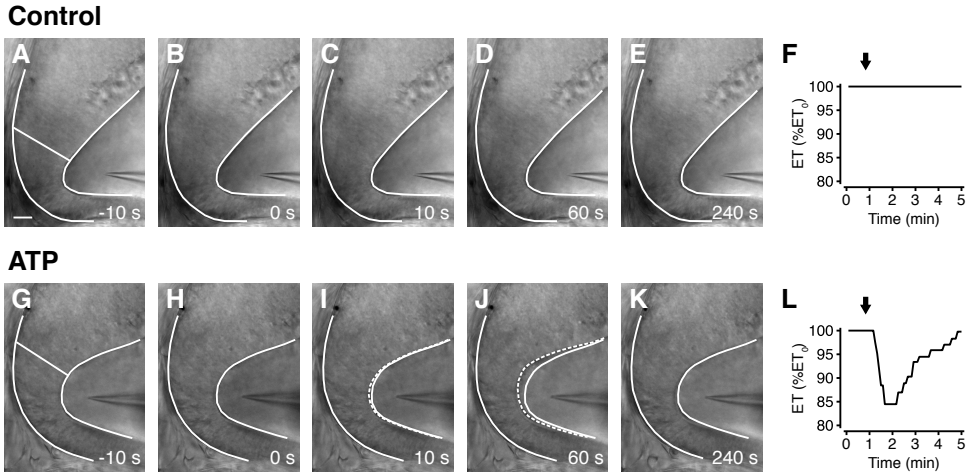
Control
A
B
C
D
E
-10 s
0 s
10 s
60 s
240 s
F
100
95
90
85
80
ET (%ET0)
0 1 2 3 4 5
Time (min)
ATP
G
H
I
J
K
-10 s
0 s
10 s
60 s
240 s
L
100
95
90
85
80
ET (%ET0)
0 1 2 3 4 5
Time (min)

SUPPLEMENTAL FIGURE LEGENDS

Figure S1. Calcium waves spread through the neuroepithelium from the location of injury, and both tissue contractions and cell expulsions operate in the developing brain until at least four months of age, Related to Figure 1

(A-L) Time series of the optic tectum loaded with OGB-1 and PI. Even though both OGB-1 and PI fluorescence were recorded, only OGB-1 is shown for clarity. The colored circles represent areas where calcium fluorescence was measured. A cell death event after mechanical injury (arrow) induces a calcium wave that spreads through the tissue from the location of injury. Scale bar represents 10 μm.

(M) Quantification of calcium transients at different distances from the location of injury. The arrow indicates the timing of cell death through mechanical injury.

(N) Onset of calcium transients in (M). Cells further away from the location of injury display increasingly later onsets.

(O,P) Quantification of contraction amplitude (O) and cell expulsions (P) at different developmental stages. $n \geq 4$ animals in each condition.

All population data are represented as mean ± sem.

Figure S2. Inducing necrotic cell death via an electrical stimulus leads to calcium waves, tissue contractions and cell expulsions, Related to Figure 2

(A) The optic tectum was loaded with the calcium indicator OGB-1 and an average of ten time frames is shown for an overview of tissue architecture. The radial line indicates where epithelial thickness was measured and the circle represents the area where fluorescence was measured. Scale bar represents 10 μm.

(B-F) Time series of the optic tectum loaded with OGB-1 and PI. A high voltage electrical stimulus is delivered with a micropipette as indicated by the egress of Alexa Fluor® 488 labeled dextran from the pipette at t = 0 s. The electrical stimulus leads to necrotic cell death (arrow), the appearance of a calcium wave, and radial contraction of the neuroepithelial tissue. Several of the dead cells are then expelled from the tissue into the ventricle. Solid white lines represent tissue outline at t = 0 s and dashed white lines represent tissue outline at the specified time.

(G) Quantification of calcium transient, tissue contraction and cell expulsion. The calcium transient measurement shows OGB-1 and Alexa Fluor® 488 fluorescence. The arrow indicates the timing of cell death through the electrical stimulus. ET, epithelial thickness. EA, expelled area.

Figure S3. Focal delivery of ATP induces tissue contractions in the tectal neuroepithelium, Related to Figure 5

(A-E) and (G-K) The optic tectum was imaged using brightfield illumination and a puff of ACSF (A-E) or ATP in ACSF (G-K) was delivered from a micropipette at t = 0 s. The radial line indicates where epithelial thickness was measured. Solid white lines represent tissue outline at t = 0 s and dashed white lines represent tissue outline at the specified time. Scale bar represents 10 μm.

(F,L) Quantification of tissue contraction from (A-E) and (G-K). Arrow indicates the timing of the puffs. ET, epithelial thickness. n ≥ 6 animals in each condition.

SUPPLEMENTAL MOVIE LEGENDS

Movie S1. A calcium wave, tissue contraction, and the expulsion of a dead cell are triggered by mechanical injury, Related to Figure 1

The optic tectum was loaded with OGB-1 (green) and PI (magenta). The tissue is then mechanically injured with a fine micropipette. One cell takes up PI immediately after the injury and is expelled into the ventricle during the neuroepithelial contraction.

Movie S2. A calcium wave, tissue contraction and the expulsion of a dead cell are triggered by high power laser scanning, Related to Figure 2

The optic tectum was loaded with OGB-1 (green) and PI (magenta). High power laser scanning of the entire field of view leads to the death of a progenitor cell, which is subsequently expelled into the ventricle. There is an additional calcium wave that originates slightly posterior to the location of the cell death event around 150 s.

Movie S3. A calcium wave, tissue contraction, and the expulsion of several dead cells are triggered by a high voltage electrical stimulus, Related to Figure 2

The optic tectum was loaded with OGB-1 (green) and PI (magenta). A high voltage electrical stimulus is delivered, which leads to cell death in the tissue and the expulsion of several cells into the ventricle during tissue contraction.

Movie S4. A control puff does not elicit a tissue response but an ATP puff induces a calcium wave and tissue contraction, Related to Figure 5

The optic tectum was loaded with OGB-1 (green). In the first experiment, a puff of ACSF with Alexa Fluor® 594 hydrazide for visualization (magenta) is delivered to the ventricular surface of the tectum but does not trigger a calcium wave or tissue contraction. In the second experiment, a puff of ATP in ACSF with Alexa Fluor® 594 hydrazide for visualization (magenta) is delivered and induces a calcium wave and tissue contraction.

Movie S5. A control puff does not elicit a tissue response but an ATP puff induces a tissue contraction, Related to Figure 5

The optic tectum is imaged using brightfield illumination. In the first experiment, a puff of ACSF with Fast Green for visualization is delivered at t = 50 s (asterisk) but does not induce contraction of the brain tissue. In the second experiment, a puff of ATP in ACSF with Fast Green for visualization is delivered at t = 50 s (asterisk), which induces a radial contraction of the brain tissue.

Movie S6. A cell death event induces reorganization of the actin cytoskeleton, tissue contraction, and cell expulsion, Related to Figure 6

The F-actin reporter GFP-UtrCH (green) was expressed in the optic tectum, and PI (magenta) was injected into the ventricle. Immediately after a cell death event, F-actin relocalizes from the apical to the basolateral region of the

neuroepithelium. This is followed by a tissue contraction and the expulsion of the damaged cell.

SUPPLEMENTAL EXPERIMENTAL PROCEDURES

Progenitor cell labeling

We used single-cell electroporation of fluorescently labeled dextran for labeling of individual progenitors and their progeny (Bestman et al., 2006; Haas et al., 2001). Briefly, a glass micropipette containing 5 mg/ml Oregon Green 10,000 MW dextran in calcium-free Ringer's solution (116 mM NaCl, 1.2 mM KCl, 2.7 mM $NaHCO_3$, 5 mM HEPES, pH 7.2) was positioned near the ventricular surface of the optic tectum. Cells were electroporated by delivering a short train of electrical pulses using an Axoporator 800A (Molecular Devices) at voltage amplitudes of 1-5 V. The labeling of individual progenitor cells was confirmed 1-3 h after electroporation. Tadpoles with single progenitor cells were returned to rearing solution and allowed to develop for 1-3 days before imaging on a confocal microscope equipped with a 488 nm argon laser (Melles Griot), a ×60 0.9 NA LUMPlanFl/IR objective (Olympus) and Fluoview FV300 image acquisition software (Olympus).

In vivo calcium imaging

For calcium imaging with Oregon Green BAPTA-1 AM (OGB-1 AM, Invitrogen) we followed established protocols (Dunfield and Haas, 2010; Niell and Smith, 2005). Briefly, the calcium indicator OGB-1 AM was solubilized in 20% Pluronic F-127 in DMSO (Invitrogen) and diluted in calcium-free Ringer's solution to yield a working concentration of 1 mM OGB-1 AM. The solution also contained 100 µM Alexa Fluor® 594 hydrazide (Invitrogen) to facilitate

visualization during loading and the dye was low pressure injected into the tectal neuropil. Tadpoles were allowed to recover in rearing solution for at least 2 h before being reanaesthetized for multiphoton imaging. Loading with calcium indicator did not affect levels of apoptosis as determined by Caspase 3 staining (1.4 ± 0.7 Caspase 3^+ cells in control animals, 1.6 ± 0.7 Caspase 3^+ cells in OGB-1 loaded animals, n ≥ 7 animals in each condition, p = 0.854 in Mann-Whitney U test), or levels of necrosis as determined by propidium iodide (PI) uptake (0.4 ± 0.1 PI^+ cells in control animals, 0.2 ± 0.1 PI^+ cells in OGB-1 loaded animals, n = 34 animals in each condition, p = 0.140 in Mann-Whitney U test).

Drug treatments

To activate ATP receptors, 100 µM ATP was dissolved in calcium-free Ringer's solution containing 100 µM Alexa Fluor® 594 hydrazide for visualization. For delivery of ATP in brightfield imaging experiments, 0.03% Fast Green was used for visualization. The solution was then focally delivered to the ventricular surface of the optic tectum using a fine micropipette. To block ATP receptors, we used a range of antagonists with different but overlapping selectivities (Figure 5M). Suramin, MRS2179, PPADS or *iso*-PPADS (all 20 mM, Tocris) in calcium-free Ringer's solution with 0.03% Fast Green were injected into the tectal ventricle, and injection was monitored using a Leica S6E dissection scope with a Leica CLS 100X Illuminator light source. Suramin is a non-selective ATP receptor blocker that inhibits a broad range of metabotropic and ionotropic ATP receptors

(Abbracchio et al., 2006; Khakh et al., 2001). In contrast, MRS2179 is selective for the $P2Y_1$ subtype of metabotropic receptors (Boyer et al., 1998). Like suramin, PPADS blocks a number of different metabotropic and ionotropic receptors (Abbracchio et al., 2006; Khakh et al., 2001). The related compound *iso*-PPADS inhibits only a small number of P2X receptors (Kim et al., 2001). In particular, it is a strong inhibitor of $P2X_1$ and $P2X_3$ receptors, where it is several fold more potent than PPADS (Brown et al., 2001; Kim et al., 2001). We obtained a significant reduction of calcium wave activity with the non-selective inhibitors suramin and PPADS (Figure 5M). These results are consistent with an involvement of both P2X and P2Y receptors, however there was no significant reduction in calcium wave activity in MRS2179-treated animals (Figure 5M), arguing against a major role for $P2Y_1$ receptors. We also detected a significant decrease in calcium wave activity with the P2X-specific inhibitor *iso*-PPADS (Figure 5M), suggesting an involvement of the $P2X_1$ or $P2X_3$ subtypes of ionotropic receptors. In summary, these results are consistent with a role for $P2X_1$ or $P2X_3$ receptors, and also with a contribution from P2Y receptors other than the $P2Y_1$ subtype.

We blocked release of calcium from intracellular stores by injecting 1 mM thapsigargin (Tocris), which depletes intracellular calcium stores, or 20 mM 2-APB, an inhibitor of IP_3-mediated calcium release, into the tectal ventricle. To assess the role of gap junctions, 1 mM carbenoxolone or 1 mM flufenamic acid, both of which are gap junction inhibitors, were injected into the ventricle.

For induction of calcium transients independently of ATP, 1 mM Ionomycin or 1 mM A23187, which act as calcium ionophores, were focally delivered to the ventricular surface of the optic tectum using a fine micropipette.

To attenuate rises in intracellular calcium, the calcium chelator BAPTA AM (Invitrogen) was solubilized in 20% Pluronic F-127 in DMSO (Invitrogen) and diluted in calcium-free Ringer's solution to a concentration of 5 mM. The working solution also contained 0.5 mM OGB-1 AM for calcium imaging and 100 µM Alexa Fluor® 594 hydrazide for visualization, and was injected into the tectal neuropil as described above. We injected 5 mM Y-27632, a Rho kinase inhibitor, into the ventricle to investigate the role of Rho kinase activation. To assess the role of actomyosin, brain explants were incubated in 50 µM blebbistatin in ACSF for 30 min before imaging and throughout the duration of the imaging protocol. To induce apoptotic cell death, animals were reared in 100 µg/ml cycloheximide in MBS.

Immunohistochemistry

Tadpoles were euthanized in 2% MS-222 and fixed in 4% paraformaldehyde for 12-16 h at 4 °C. After fixation, brains were excised, rinsed in phosphate buffered saline (PBS), blocked for 1-4 h at room temperature in blocking solution (1% BSA, 1% DMSO, 0.5% Triton X-100, 0.01% sodium azide in PBS) and incubated in rabbit anti-Caspase 3 antibody (BD Pharmingen 559565, 1:500) in blocking solution for 12-16 h at 4 °C. This antibody has been previously reported to detect apoptotic cells in the brain of *Xenopus*

laevis tadpoles (Kaya et al., 2012). Brains were then rinsed in PBS with 0.5% Triton X-100 for 2-4 h at room temperature, incubated in Alexa Fluor® 488 anti-rabbit IgG antibody (Invitrogen A11034, 1:500) in blocking solution for 12-16 h at 4 °C, and rinsed in PBS. For detection of cell nuclei, brains were incubated in PBS with 1 µg/ml PI and 100 µg/ml RNAse A (Roche) for 30 min at 37 °C and rinsed in PBS before mounting and imaging. Images were collected on a confocal microscope equipped with a 488 nm argon laser (Melles Griot), a 543 nm helium-neon laser (Showa Optronics), a ×60 0.9 NA LUMPlanFl/IR objective (Olympus) and Fluoview FV300 image acquisition software (Olympus).

Quantitative analysis of calcium signaling and tissue dynamics

For quantitative analysis of calcium signaling, time series of images were saved as TIFF stacks and registered using the StackReg plugin in ImageJ (http://rsbweb.nih.gov/ij) to correct for xy drift. The coordinates of individual cell bodies were manually identified and dF/F traces for each cell were calculated from the mean pixel intensity of a 3 µm diameter circle about the cell's center using custom-written scripts in MATLAB (Mathworks). A calcium transient was defined as an event in which dF/F crossed a threshold of two to four times the standard deviation of the cell's mean dF/F for a period of at least 10 s. A calcium wave was defined as an event in which a minimum of four adjacent cells experienced a calcium transient within 15 s of each other. The amplitude of a calcium wave was calculated as the mean amplitude of the

transients in all participating cells. The size of a calcium wave was defined as the number of participating cells.

For quantification of tissue contractions, epithelial thickness (ET) was measured from calcium or brightfield imaging data, and a tissue contraction was defined as an event where ET was decreased for at least 20 s before gradually recovering. ET was measured at the center of its associated calcium wave. Contraction amplitude was calculated as the difference between the average ET during the 50 s preceding calcium wave onset and the minimum ET observed during the contraction.

For quantification of the movement of cell nuclei during tissue contractions, the centers of nuclei labeled with Hoechst nucleic acid dye were manually traced over time and the distance between pairs of nuclei was calculated using a custom-written script in MATLAB. The reduction in distance between nuclei was calculated as the difference between the distance before contraction onset and the minimum distance observed during peak tissue contraction.

For quantification of cell geometry during tissue contractions, the length and width of progenitor cells were measured manually over time. The reduction in the ratio of cell length to width was calculated as the difference between the ratio before contraction onset and the minimum ratio observed during peak tissue contraction.

For quantification of expulsion speed and size, we measured the expelled area (EA) of a cell over time from the start of expulsion until 200 s after expulsion onset using PI imaging data acquired simultaneously with

calcium imaging data. Expulsion speed was calculated as the mean increase in EA during the first 50 s of the expulsion event, and expulsion size was calculated as the mean EA from 50 - 200 s following expulsion onset.

For quantification of GFP-UtrCH fluorescence, we defined Region 1 as the area between 0 and 2 μm from the ventricular surface, and Region 2 as the area between 2 and 10 μm from the ventricular surface. Fluorescence in Regions 1 and 2 was measured as the mean gray value in a box with a lateral extent of 20 μm centered on the location of cell death, or in two boxes which were centered on positions at a distance of 50 μm along the ventricular wall on either side of the location of cell death.

Analysis of spatial distribution of PI^+ cells

To investigate the spatial distribution of PI^+ cells (Figure 8B), we used a bootstrap analysis in MATLAB where we first calculated the mean nearest neighbor distance for each PI^+ cell (n = 13 animals). For each animal, we then generated 10,000 sets of PI^+ cells that were randomly distributed in tectal space such that the number of cells matched those in the experimental data, and calculated their mean nearest neighbor distances. The p value reported for this analysis corresponds to the proportion of mean nearest neighbor distances from the random data set that was smaller than the mean nearest neighbor distances from the experimental data.

SUPPLEMENTAL REFERENCES

Bestman, J.E., Ewald, R.C., Chiu, S.-L., and Cline, H.T. (2006). In vivo single-cell electroporation for transfer of DNA and macromolecules. Nature Protocols *1*, 1267–1272.

Boyer, J.L., Mohanram, A., Camaioni, E., Jacobson, K.A., and Harden, T.K. (1998). Competitive and selective antagonism of P2Y1 receptors by N6-methyl 2'-deoxyadenosine 3‘,5’-bisphosphate. Br. J. Pharmacol. *124*, 1–3.

Brown, S.G., Kim, Y.-C., Kim, S.A., Jacobson, K.A., Burnstock, G., and King, B.F. (2001). Actions of a series of PPADS analogs at P2X1 and P2X3 receptors. Drug Development Research *53*, 281–291.

Dunfield, D., and Haas, K. (2010). In vivo single-cell excitability probing of neuronal ensembles in the intact and awake developing Xenopus brain. Nature Protocols *5*, 841–848.

Haas, K., Sin, W.-C., Javaherian, A., Li, Z., and Cline, H.T. (2001). Single-Cell Electroporation for Gene Transfer In Vivo. Neuron *29*, 583–591.

Kaya, F., Mannioui, A., Chesneau, A., Sekizar, S., Maillard, E., Ballagny, C., Houel-Renault, L., Dupasquier, D., Bronchain, O., Holtzmann, I., et al. (2012). Live imaging of targeted cell ablation in Xenopus: a new model to study demyelination and repair. J. Neurosci. *32*, 12885–12895.

Kim, Y.C., Brown, S.G., Harden, T.K., Boyer, J.L., Dubyak, G., King, B.F., Burnstock, G., and Jacobson, K.A. (2001). Structure-activity relationships of pyridoxal phosphate derivatives as potent and selective antagonists of P2X1 receptors. J. Med. Chem. *44*, 340–349.

Niell, C.M., and Smith, S.J. (2005). Functional imaging reveals rapid development of visual response properties in the zebrafish tectum. Neuron *45*, 941-51.